Electronic Supplementary Information

From single-site tantalum complexes to nanoparticles of Ta_xN_y and TaO_xN_y supported on silica: Elucidation of synthesis chemistry by dynamic nuclear polarization surface enhanced NMR spectroscopy and X-ray absorption spectroscopy

Janet C. Mohandas,[a] Edy Abou-Hamad,[‡a] Emmanuel Callens,[‡a] Manoja K. Samantaray,[a] David Gajan,[b] Andrei Gurinov,[a] Tao Ma,[c] Samy Ould-Chikh,[a] Adam S. Hoffman,[c] Bruce C. Gates*[c] and Jean-Marie Basset.*[a]

[a] King Abdullah University of Science & Technology, KAUST Catalysis Center (KCC), 23955-6900 Thuwal, Saudi Arabia,

[b] Institut de Sciences Analytiques (CNRS / ENS-Lyon / UCB-Lyon 1), Université de Lyon, Centre de RMN à Très Hauts Champs, 69100 Villeurbanne, France,

[c] Department of Chemical Engineering, University of California, Davis, CA 95616, USA, California 95616, USA.

CONTENTS

Experimental Procedures

General procedure

All experiments were carried out by using the standard air-free methodology in an argon-filled glove box, on a Schlenk line, or in a Schlenk-type apparatus interfaced to a high-vacuum line (10^{-6} mbar). Anhydrous $TaCl_5$ powder (99.999% trace metal basis), dimethyl zinc solution- (1 M in heptane) and methyl lithium solution (1.6 M in diethyl ether) were purchased from Sigma-Aldrich. Dry pentane collected from the SPS (solvent purification system) was degassed by freeze pump thaw cycles. $Ta(OMe)_5$ (99.99%) used as a precursor was obtained from Strem chemicals.

Preparation of SiO_2-700

A mass of 3 g of Aerosil SiO_2 200 (Degussa) (BET surface area: 200 m^2/g) was first compacted by adding deionized water and dried in an air oven maintained at 393 K overnight. The dried powder was ground nicely and then calcined in a double-sided tubular reactor fitted with a silica frit in the middle under a flow of air at 673 K for 4 h. Calcined silica is then transferred to a quartz batch reactor fitted with an adaptor to connect to a high vacuum line. After evacuating the reactor, partial dehydroxylation step was carried out at 973 K for 16 h. The as-synthesized material is denoted as SiO_2-700. BET surface area of SiO_2-700 is ~182 m^2/g (BJH method) and its adsorption average pore volume is around 1.35 cm^3/g.

Preparation of $TaMe_5$ (1) and (≡SiO)$TaMe_4$ (1A)

$TaMe_3Cl_2$ was prepared by using a reported procedure[1]. Under argon atmosphere, $TaMe_3Cl_2$ (1 mmol) was added into one compartment of a chilled (at 195 K) double-Schlenk tube with 15 ml of dry pentane, after stirring for 5 min, (4.5 mmol, excess) MeLi powder was added to the suspension. The reaction mixture was stirred for 1 h and allowed the temperature of the bath to reach 243 K. The reaction mixture turned bright yellow and the stirring continued for another hour until the temperature warmed up to 253 K. The solution was then filtered to the other side of the double-Schlenk to collect a solution of $TaMe_5$.[2] This solution is then transferred to another double Schlenk, maintained at 253 K, where 3 g of SiO_2-700 was stirred in 10 ml of dry pentane. This solution was stirred for an hour while the bath was warming up to 243 K. The excess solvent, pentane, was decanted off and the dull white solid was dried under high vacuum (<10^{-6} mbar) to remove any traces of pentane. The compound was stored at 233 K in a freezer inside a glove box. ^{1}H NMR δ 0.8 ppm (Ta-C$\boldsymbol{H}_3$) and ^{13}C NMR δ 73 ppm (Ta-$\boldsymbol{C}$H$_3$). Elemental analysis gave Ta 4.1%, C 0.98%, H 0.24% with a C/Ta value ~3.6±0.3. **Caution:** One should note that this precursor is unstable and gives a dark grey compound if it is exposed to light or stored at room temperature for long hours.

Preparation of [(≡SiO)$TaOMe_4$] (1B)

A 500 ml glass reactor is loaded with 200 mg of **1A** under controlled atmosphere, followed by its evacuation at high vacuum line (<10^{-6} mbar). The reactor is then exposed to 1 bar of dry O_2 (99.9999%) and allowed to react for 15 h at room temperature. The gas phase is then evacuated and the as-synthesized material is denoted as **1B**.

Preparation of [(≡SiO)$TaOMe_4$] (2A)

---

[1] G. L. Juvinall, *J. Am. Chem. Soc.*, 1964, **86**, 4202-4203.;

[2] R. R. Schrock and P. Meakin, *J. Am. Chem. Soc.*, 1974, **96**, 5288-5290.

Commercial precursor $Ta(OMe)_5$ **(2)** (99.99 %) was obtained from Strem chemicals and grafted on SiO_2-700 to prepare **2A**. Grafting was carried out in pentane solution at room temperature in a double-Schlenk. A mass of 101 mg of $Ta(OMe)_5$ and 1 g of SiO_2-700 were used. The mixture was allowed to stir for 3 h. The solvent was then decanted and discarded. The grafted complex was dried under high vacuum ($<10^{-6}$ mbar) to remove any traces of remaining pentane.

Preparation of Ta_xN_y/TaO_xN_y nanoparticles

As-synthesized precursors, **1B** and **2A**, were subjected to NH_3 treatment for the synthesis of Ta_xN_y/TaO_xN_y nanoparticles (**1C** and **2B**). Detailed procedure is as follows. A mass of 1 g of precursor (**1B**) or (**2A**) was loaded in a double-sided quartz reactor in an argon-filled glove box. The reactor was then transferred to a horizontal tubular furnace in dynamic flow of nitrogen to avoid any exposure to air. N_2 flow was then replaced by 200 ml/min of NH_3 (99.9999%) using a switch valve. The furnace was then heated to 1173 K and the temperature was maintained for 15 h before cooling down to room temperature. The sample was collected, analyzed and used directly for the catalytic activity studies.

Catalytic activity studies

Catalytic epoxidation of cyclooctene using H_2O_2 was carried out in a 25 ml round bottom (RB) flask in an oil bath maintained on a hot plate with magnetic stirrer, fitted with a reflux condenser and a thermometer. A temperature controller controlled the temperature of the bath. Reaction conditions are as follows: Substrate/cyclooctene (0.92 ml); catalyst (4-70 mg) ; solvent/methanol (4 ml) and oxidant/30 wt.% H_2O_2 (3 ml). Catalyst/substrate/oxidant ratio maintained was in the order of 1/10,000/100,000. Reactions were carried out at 333 K for 18 h. A definite amount of reaction mixture was withdrawn after the reaction. The products formed were analyzed quantitatively by GC-FID equipped with a capillary column. The identification of products was achieved by the retention time of the pure compounds. The conversion was measured as a function of reaction time. Blank experiments were also conducted in the absence of catalyst and/or peroxide. The activities are reported as turn over numbers per Ta content (in mol) of the catalyst used. Experiments were carried out in duplicates.

Characterization Techniques

(a) Liquid State Nuclear Magnetic Resonance spectroscopy

All liquid state NMR spectra were recorded on Bruker Avance 600 MHz spectrometers. All chemical shifts were measured relative to the residual ^1H or ^{13}C resonance in the deuterated solvent: CD_2Cl_2.

(b) Solid State Nuclear Magnetic Resonance spectroscopy

One dimensional ^1H MAS and ^{13}C CP MAS solid state NMR spectra were recorded on Bruker AVANCE III spectrometers operating at 400 MHz or 600 MHz resonance frequencies for ^1H. 400 MHz experiments employed a conventional double resonance 4 mm CP MAS probe, while experiments at 600 MHz utilized a 3.2 mm HCN triple resonance probe. In all cases, the samples were packed into rotors under inert atmosphere inside gloveboxes. Dry nitrogen gas was utilized for sample spinning to prevent degradation of the samples. NMR chemical shifts are reported with respect to the external references TMS and adamantane. For ^{13}C CP MAS NMR experiments, the following sequence was used: 90^0 pulse on the proton (pulse length 2.4 s), then a cross-polarization step with a contact time of typically 2 ms, and finally acquisition of the ^{13}C signal under high power proton decoupling. The delay between the scans was set to 4 s to allow the complete relaxation of the ^1H nuclei and the number of scans ranged between 5000 – 10000 for ^{13}C and was 8 for ^1H. An exponential apodization function corresponding to a line broadening of 80 Hz was applied prior to Fourier transformation.

(c) Dynamic Nuclear Polarization NMR spectroscopy (DNP SENS)

Sample Preparation

TEKPol was dried under high vacuum (10^{-4} mbar) and the solvents were stirred over calcium hydride and then distilled in vacuo. A radical solution consisting of 16 mM TEKPol (TEKPol, MW= 905 g/mol) in either 1,1,2,2-tetrachloroethane (TCE) or 1,2-dichlorobenzene (DCB) was used. The SOMC compounds and the corresponding nitrides synthesized were finely ground in a mortar and pestle prior to preparation of DNP experiments. DNP samples were then prepared by incipient wetness impregnation. In a typical experiment, 15 mg of the samples were impregnated with the appropriate volume of 16 mM solution of TEKPol (n_{TEKPol} = 0.5 - 1.2 µmol/sample) and packed into a 3.2 mm o.d. sapphire rotor capped with a teflon plug under argon atmosphere. The packed samples were then immediately inserted into the pre-cooled DNP probe for experiments.

Measurements

Data were acquired at Core Lab of King Abdullah University using 263 GHz/400 MHz Avance III Bruker DNP solid-state NMR spectrometer equipped with a 3.2 mm Bruker triple resonance low temperature magic angle spinning (LTMAS) probe and the experiments were performed at ca. 100 K with a 263 GHz gyrotron. The sweep coil of the main magnetic field was set for the microwave irradiation occurring at the ^{1}H positive enhancement maximum of the TEKPol biradical.

^{13}C CP MAS DNP SENS

For ^{13}C NMR experiments the acquisition parameters used are 3 s repetition delay, a ^{1}H $\pi/2$ pulse length of 2.5 µs to afford 100 kHz ^{1}H decoupling using the SPINAL 64 method. The contact time was typically 3 ms for cross polarization experiments. The MAS frequency varied between 8 and 12 kHz. The two-dimensional (2D) ^{1}H-^{13}C heteronuclear correlation (HETCOR) spectra was acquired with 2048 scans per t_1 increment, 96 individual increments and 0.2 ms contact time. During t_1, e-DUMBO-1 homonuclear ^{1}H decoupling was applied and proton chemical shifts were corrected by applying a scaling factor of 0.57[3]. All ^{13}C NMR spectra were referenced to adamantane with the higher frequency peak set to 60 ppm with respect to TMS (0 ppm). More detailed information can be obtained from Table S1.

^{29}Si CP MAS DNP SENS

For ^{29}Si NMR experiments the acquisition parameters used are 3 s repetition delay, a ^{1}H $\pi/2$ pulse length of 2.5 µs to afford 100 kHz ^{1}H decoupling using the SPINAL 64 method. The contact time was typically 5 ms for cross polarization experiments. The MAS frequency varied between 8 and 12 kHz. The two-dimensional (2D) ^{1}H-^{29}Si heteronuclear correlation (HETCOR) spectra was acquired with 2048 scans per t_1 increment, 96 individual increments and 0.2 ms contact time. During t_1, e-DUMBO-1 homonuclear ^{1}H decoupling was applied and proton chemical shifts were corrected by applying a scaling factor of 0.57[3].All ^{29}Si NMR spectra were referenced to TMS (0 ppm). More detailed information can be obtained from Table S1.

^{15}N CP MAS DNP SENS

For ^{15}N NMR experiments the acquisition parameters used are 3 s repetition delay, a ^{1}H $\pi/2$ pulse length of 2.5 µs to afford 100 kHz ^{1}H decoupling using the SPINAL 64 method. The contact time was typically 4 ms for cross polarization experiments. The MAS frequency varied between 8 and 12 kHz. The two-dimensional (2D) ^{1}H-^{15}N heteronuclear correlation (HETCOR)

---

[3] B. Elena, G. de Paëpe and L. Emsley, *Chem. Phys. Lett.*, 2004, **398**, 532-538.

spectra was acquired with 2048 scans per t_1 increment, 96 individual increments and 4 ms contact time. During t_1, e-DUMBO-1 homonuclear ^1H decoupling was applied and proton chemical shift were corrected by applying a scaling factor of 0.57[3]. All ^{15}N NMR spectra were referenced to NH_4^+ resonance of ammonium nitrate (δ_{iso}= 0 ppm) by using ^{15}N labled proline dissolved in a 12 mM TOTAPOL solution in $^2H_2O/H_2O$/glycerol mixture as secondary external reference. More detailed information can be obtained from Table S1.

Processing

DNP enhancements were determined by comparing the integration of the resonance of interest for the spectra acquired with and without microwave.

Table S1 Acquisition parameters for the double resonance probe.

Pulse Sequence	**Hahn-Echo**	**CP MAS**	**HETCOR**	**CP MAS**	**HETCOR**	**CP MAS**	**HETCOR**
Nuclei	^1H	^{13}C	^1H-^{13}C	^{29}Si	^1H-^{29}Si	^{15}N	^1H-^{15}N
µwave on/ µwave off	**µwave on/ µwave off**						
Number of Scans	16	128-1024	128	1024/10240	80	128-3072	128
Recycle Delay (s)	3	3	3	3	3	3	3
Dwell (µs)	6.5	16.8	16.8	12.0	12.0	12.0	12.0
Spectral width (kHz)	10	20	20	20	20	20	20
Spinning Speed (kHz)	8.0	8.0	8.0	8.0	8.0	8.0	8.0
Acquisition length (number of points)	1024	2048	2048	2048	2048	2048	2048
^1H 90 degree pulse width ($\pi/2$) (µs)	2.5	2.3	2.3	2.3	2.3	2.3	2.3
Contact pulse length (ms)	-	3	0.2	5	0.2	4	4
^1H rf field during contact pulse (kHz)	-	100	100	100	100	100	100
X rf field during contact pulse (kHz)	100	100	100	100	100	100	100
^1H rf field during SPINAL-64 decoupling (kHz)	-	100	100	100	100	100	100

(d) Infra-red spectroscopy

All the IR spectra were recorded on pellets made out of ~30 mg of the sample. The pellet was then placed in a sample holder which can be loaded into an IR Cell made of pyrex glass fitted with CaF_2 windows. IR cell is designed in such a way that the measurements can be carried out either in vacuum or in controlled atmospheres. Infrared spectra were recorded on a Thermo Scientific Nicolet 6700 FT-IR spectrometer typically accumulating 16 scans for each spectrum with a resolution of 4 cm^{-1}.

(e) UV-Visible diffuse reflectance spectroscopy

The optical properties of the powder samples were studied by diffuse-reflectance ultraviolet–visible (DR–UV–vis) spectroscopy performed on a JASCO model V-670 spectrophotometer equipped with an integrating sphere. The spectra were scanned from 1100 to 200 nm using halogen and deuterium lamps as the light sources. Contributions from scattering were removed using the Kubelka–Munk function. The spectra were referenced to a Spectralon standard (Lab sphere, Inc.), which reflects >99% of light in the 250–2000 nm range. Determination of the Kubelka–Munk function, $F(R_\infty)$, was obtained from the UV–vis absorbance, and the bandgap energy (E_g) was determined by finding the intercept of the straight line in the low-energy region of a plot of $[F(R_\infty)hv]^n$ vs hv, where $n = 2$ and 0.5 for the direct and indirect allowed transitions, respectively, and hv is the energy of the incident photons.

(f) X-Ray diffraction

X-Ray diffraction (XRD) on powders was carried out with a Bruker D8 Avance diffractometer (33 kV & 45 mA) with CuKα radiation ($\lambda = 0.154$ nm). The diffraction patterns were collected in the 2θ angle range [10 - 90°] at a scanning rate of 0.1°/min.

(g) XPS measurements

X-ray photo electron spectral studies were conducted using a Kratos Axis Ultra DLD spectrometer equipped with a monochromatic Al Kα X-ray source (hα = 1486.6 eV) operating at 150 W, a multi-channel plate and a delay line detector under a 1.0×10^{-9} Torr vacuum. The survey and high-resolution spectra were collected at fixed analyzer pass energies of 160 and 20 eV, respectively. The XPS spectra were analyzed using the relative sensitivity factor (RSF) method directly implemented in the software (Casa XPS). The backgrounds of the spectra were subtracted using a Shirley background or simply a linear background, and the spectra were fitted with a Gaussian–Lorentzian function. Although the Ta 4f signal is known to overlap with the minor O 2s signal, the contribution from O was neglected in this study.

(h) Transmission electron microscopy

Conventional TEM micrographs were performed using a Titan. The samples were prepared both by dispersing a drop of the ethanol suspension of the sample on a Cu grid covered by a carbon film. Aberration-corrected high-angle annular dark-field scanning transmission electron microscopy (HAADF-STEM) was performed on a Titan G2 60–300 CT electron microscope at an accelerating voltage of 300 kV. The electron gun was used in the unfiltered mode, and the probe size during STEM analysis was estimated to be approximately 0.5 nm with a beam current of 0.08 nA. Several low- and high-resolution electron micrographs were acquired from various locations during the analysis. The high-resolution transmission electron microscope (HRTEM) used is a spherical aberration corrected ETEM (Titan ETEM 80-300, FEI Company) with a point resolution of 0.09 nm in high vacuum mode.

(i) Nitrogen adsorption-desorption measurements

Niitrogen adsorption and desorption measurements were performed at 77 K using an ASAP 2020 Micromeritics system. Prior to analysis, the samples were degassed overnight at 423 K and 6.6 Pa. The pore size distribution and the mean pore size were calculated using the Barrett–Joyner–Halenda (BJH) method. The specific surface area was calculated with the Brunauer–Emmett–Teller (BET) equation. The BET surface area was determined by a multipoint BET method using the adsorption data in the relative pressure (P/P_0) range of 0.01–1.

(j) Elemental analyses

Elemental analyses of carbon, hydrogen, nitrogen, and oxygen were conducted at the Mikroanalytisches Labor Pascher in Remagen-Bandorf, Germany. The total amounts of carbon and hydrogen were determined using a C/H analyzer. The nitrogen content was determined using the hot carrier gas extraction method and a nitrogen analyzer. The oxygen content was determined using the hot vacuum extraction method and a Balzers Exhalograph EAO-202. The tantalum content was determined by inductively coupled plasma-atomic emission spectrometry (ICP-AES) using a Thermo iCap 6500. Prior to analysis, each sample was decomposed in an acid mixture of nitric acid and hydrofluoric acid (under pressure and high temperature).

(k) **EXAFS measurements**

The X-ray absorption spectroscopy (XAS) experiments were carried out at X-ray beamline 4-1 at the Stanford Synchrotron Radiation Light source (SSRL). The storage-ring electron energy was 3.0 GeV. The cryogenic double-crystal monochromator, Si(220) $\phi = 0$, was detuned by 20–30% at the Ta L_3 edge (9881 eV) to minimize higher-order harmonics present in the X-ray beam. The mass of each sample was calculated to yield optimal absorption measurements at the Ta L_3 edge (giving an X-ray absorbance of approximately 2.0 calculated at an energy 50 eV greater than the absorption edge), on the basis of the tantalum content and the cell dimensions. The sample was pressed into a wafer in an Ar-filled glovebox with < 1 ppm moisture and < 1 ppm O_2, and mounted in a specially designed cell[4] that allows collection of static XAS under high vacuum at liquid-nitrogen temperature, without exposure of the sample to air or moisture. Spectra were collected in transmission mode. A zinc reference foil was simultaneously scanned with the sample to calibrate the energy shift. The calibration was done by shifting the Zn K edge determined from the reference Zn foil to 9659 eV. Because the K edge of Zn is ~200 eV lower than Ta L_3 edge, there may still be a slight energy shift after calibration. As a result, the determination of the edge position for the spectra of the samples may not be quite accurate; hence, the values of the inner potential correction (ΔE_0) in the fitted models may be slightly out of the appropriate range.

(l) **Gas chromatography**

Quantitative analysis of products of catalysis reaction was performed on a Hewlett-Packard 5890 series II gas chromatograph equipped with a flame ionization detector and Al_2O_3/KCl on fused silica column (50 m X 0.32 mm) using an internal standard technique. A qualitative analysis of the products was carried out on an Agilent GC-MS equipped with HP-5 capillary column.

---

[4] Jentoft, R. E.; Deutsch, S. E.; Gates, B. C. *Rev. Sci. Instrum.* 1996, **67**, 2111.

Supplementary Schemes, Figures and Tables

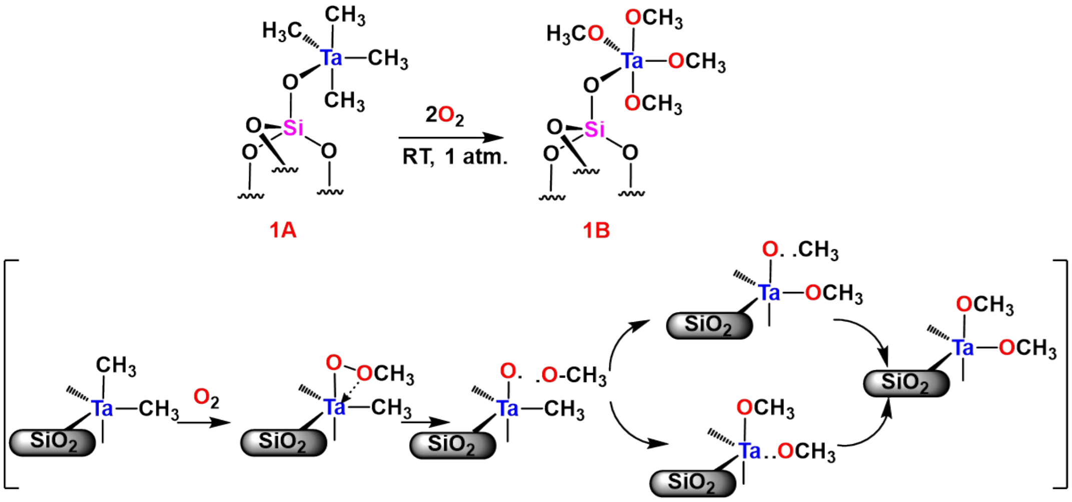

Scheme S1. A plausible pathway for oxygen insertion

Above scheme depicts a plausible pathway for O_2 insertion. We find the above-depicted pathway more suitable for the tantalum alkyls with a d^0 configuration. DFT studies by Tom Cundari *et al.* showed that complexes will effect metal-methyl oxygen-insertion either through a single-step, non-redox Baeyer-Villiger (BV) pathway or a two-step, redox oxy-insertion (oxygen atom transfer (OAT) followed by an alkyl migration. Their results suggest that while the BV mechanism is preferred by either a full (d^{10}) or empty (d^0) d-shell, the OAT pathway is operative for those metals with partially-filled d orbitals. In order to understand the exact mechanistic details, many further experiments are needed.[5]

---

[5] 1). S. C. Hunter, S.-J. Chen, C. A. Steren, M. G. Richmond and Z.-L. Xue, *Organometallics*, 2015, **34**, 5687-5696. 2). D. C. Bradley, R. C. Mehrotra, I. P. Rothwell and A. Singh, in *Alkoxo and Aryloxo Derivatives of Metals*, Academic Press, London, 2001, DOI: http://dx.doi.org/10.1016/B978-012124140-7/50002-5, pp. 3-181. 3). E. C. Garrett, III, T. M. Figg and T. R. Cundari, 2013. 4). E. C. Garrett, T. M. Figg and T. R. Cundari, *Inorg. Chem.*, 2014, **53**, 7789-7798; 5) S.-J. Chen and Z.-L. Xue, *Organometallics*, 2010, **29**, 5579-5584.

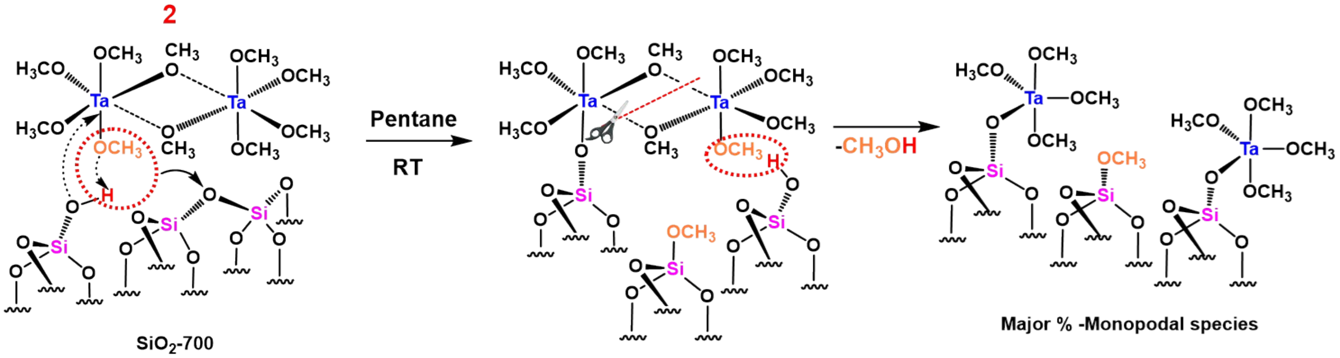

Scheme S2 Schematic representation of grafting of [Ta(OMe)$_5$] (**2**) dimer onto SiO$_2$-700 forming monomeric species

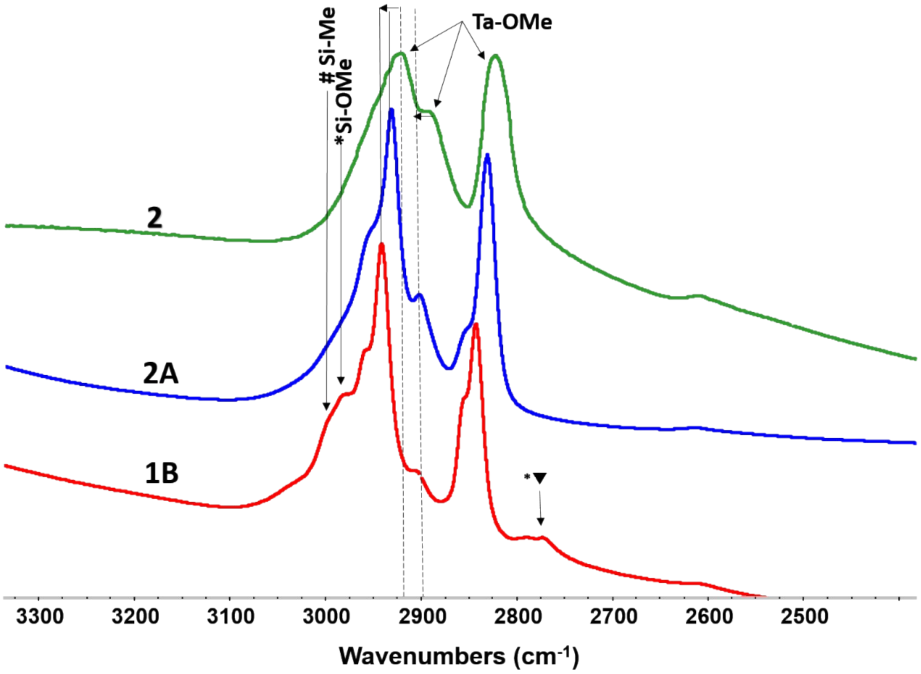

Fig. S1 Magnified region of the IR spectra given in Fig. 1 showing the formation of similar surface species in 2A and 1B. 10-20 cm^{-1} shift is observed upon grafting 2 on to the surface of SiO$_2$-700 as shown in the case of grafted complexes- 2A and 1B. *❑- corresponds to the symmetric stretching vibrations of Si-CH$_3$ or residual Ta-CH$_3$.

Table S2. Elemental analyses results for precursor complexes and NPs obtained from ICP-OES and CHN analyses.

Sample information	**Ta** (Wt. %) (±0.2)	**C** (Wt. %) (±0.3)	**N** (Wt. %) (±0.3)	C/Ta (±0.3)	N/Ta (±0.3)
1B	4.1	0.98	N/A	3.6 (4)*	N/A
2A	4.67	1.42	N/A	4.6 (5)*	N/A
1C	4.2	0.03	3.49	0.10	10.56
2B	4.8	0.05	2.97	0.15	8

*Theoretical value expected given in parenthesis;
Samples for elemental analysis were handled under controlled atmospheres

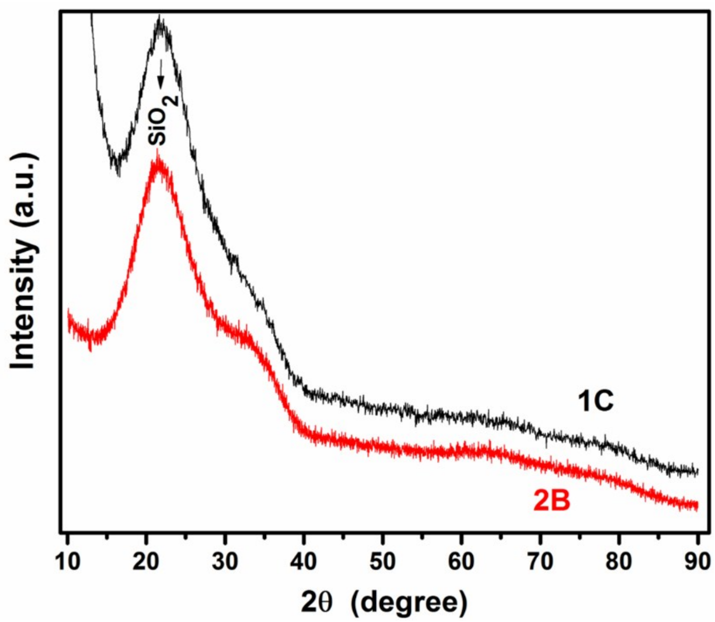

Fig. S2. Powder XRD patterns of **1C** and **2B**

X-ray diffraction patterns of **1C** and **2B** are given in Fig. S2. The broad peak at 2θ value ~22° matches the pattern of the amorphous SiO_2 of the support (Aerosil-200). The XRD patterns of both samples did not show any peaks corresponding to that of any phases of Ta_3N_5 or TaON. This might probably be due to the too low loading, amorphous nature and/or the very small size of the particles.

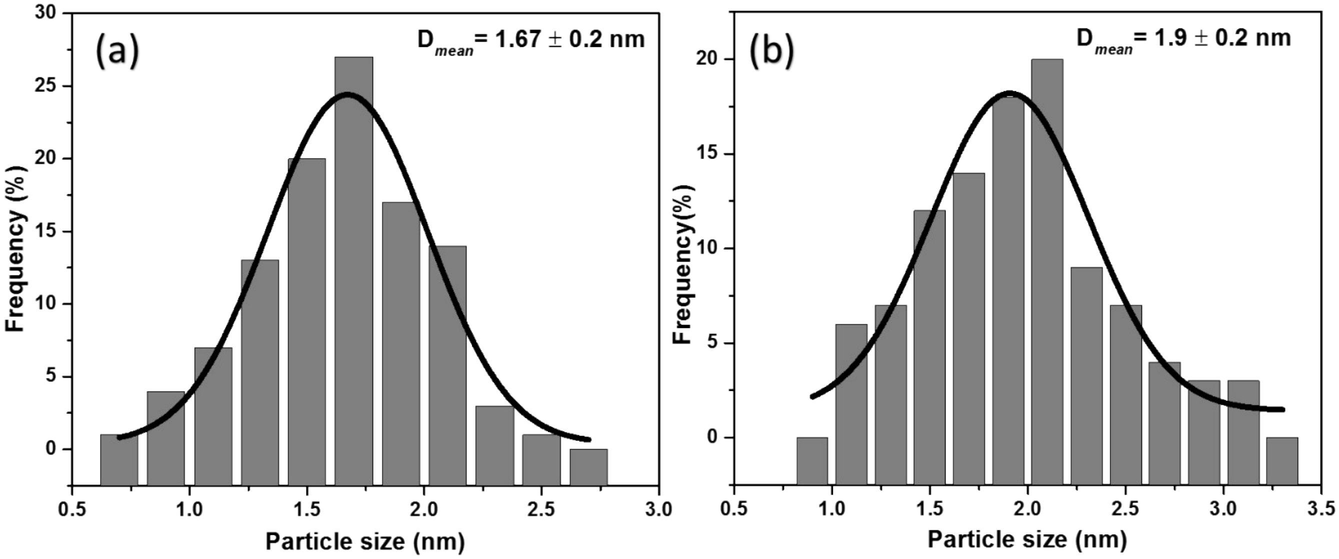

Fig. S3 Particle size distributions obtained from TEM images of (a) **1C** and (b) **2B**

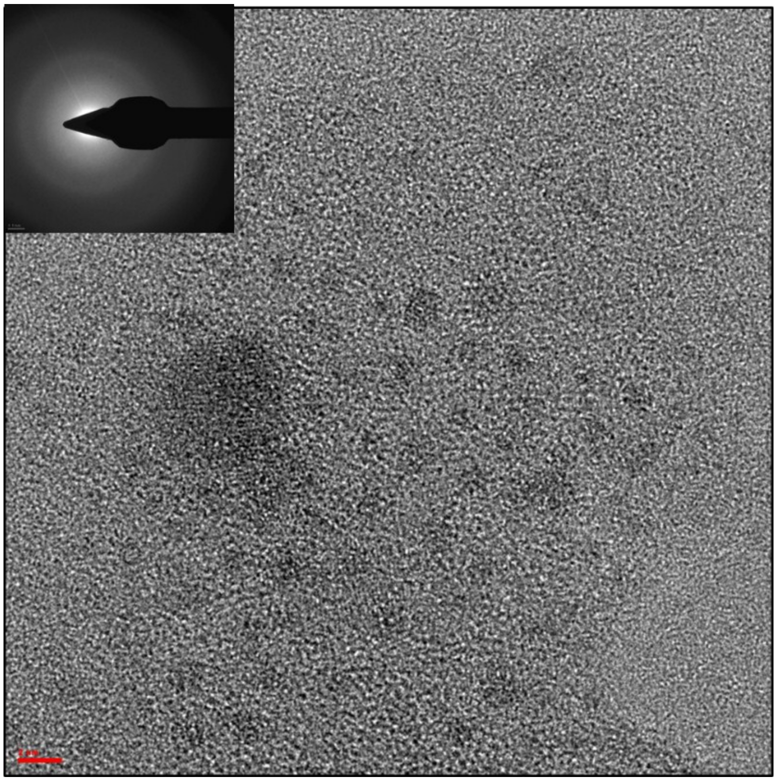

Fig. S4 HRTEM image of **1C** showing dispersed NPs. We found that the nearby fine clusters were moving on the surface and coalesce under the high energy electron beam during imaging. Inset shows the electron diffraction pattern of such a big cluster showing amorphous nature. (**Scale bar is 2 nm**)

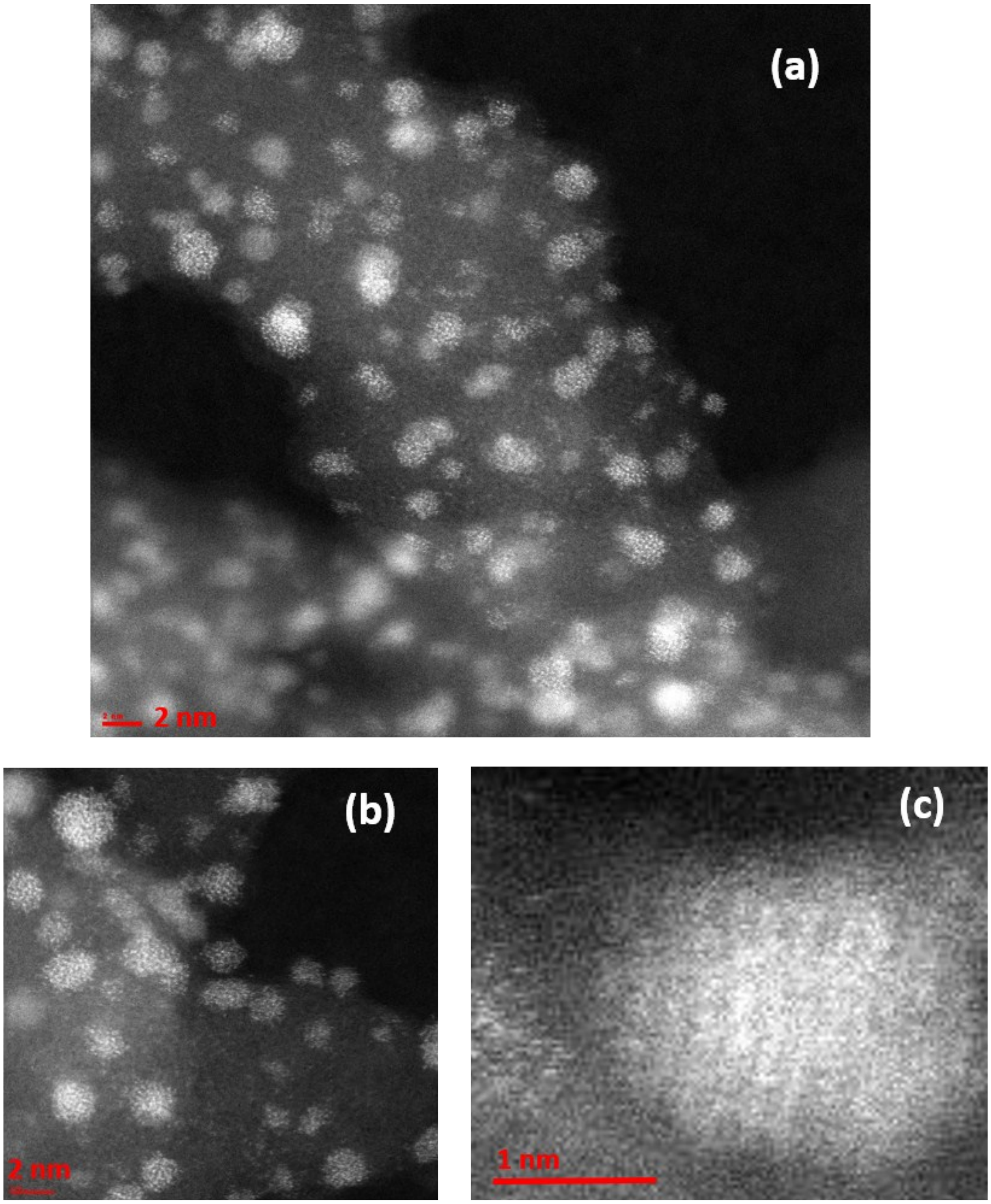

Fig. S5 High magnification STEM image of **2B** showing the small amorphous NPs((a) & (b)) and a weak short range ordering of atoms in one such amorphous NPs(c).

Table S3 provides the corresponding textural properties such as surface area, pore volume and pore size. Dehydroxylated SiO_2-700 has lost 10-15% of surface area during dehydroxylation and heating.

Table S3. Textural properties of **1C** and **2B** obtained from BET surface area measurements

Sample	$^{a}S_{BET}$ (m^2/g)	$^{b}V_{pa}$ (cm^3/g)	$^{c}D_{pa}$ (nm)
1C	171	1.46	38
2B	156	1.47	43
SiO_2 -700	182	1.35	34

[a]: BET surface area; [b]: BJH adsorption average pore volume; [c]:BJH adsorption average pore size

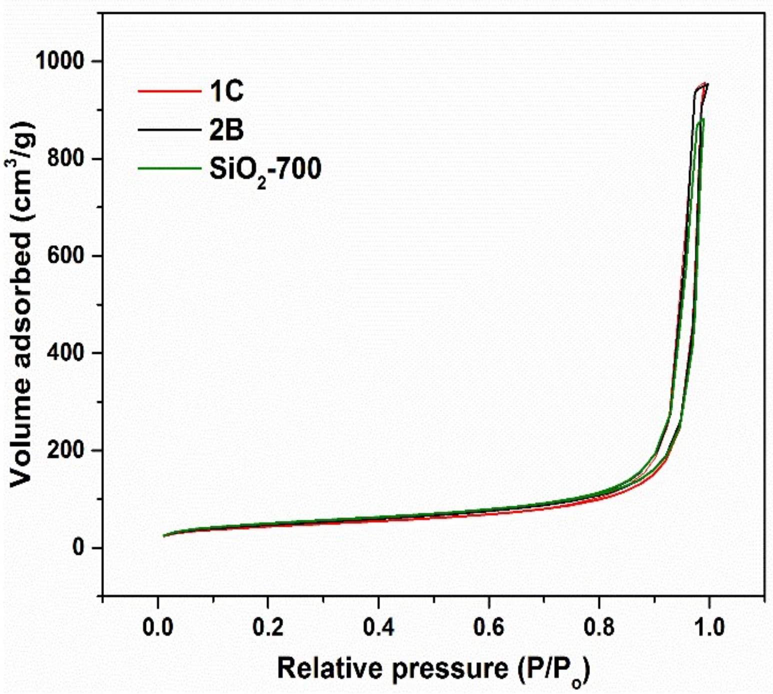

Fig. S6 N_2 adsorption-desorption isotherms of (a) **1C**, (b) **2B** and (c) SiO_2-700

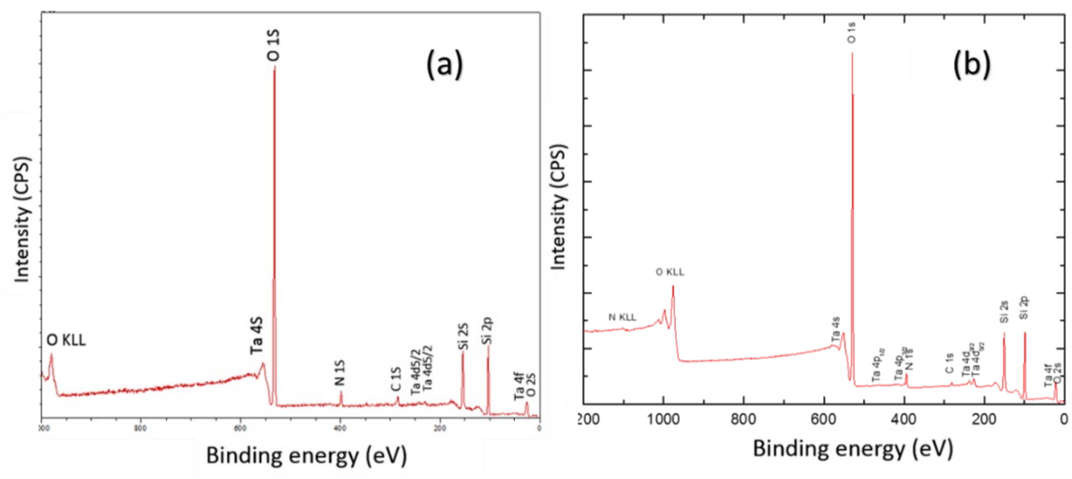

Fig. S7 X-ray photoelectron survey spectra of (a)**1C** and (b)**2B**.

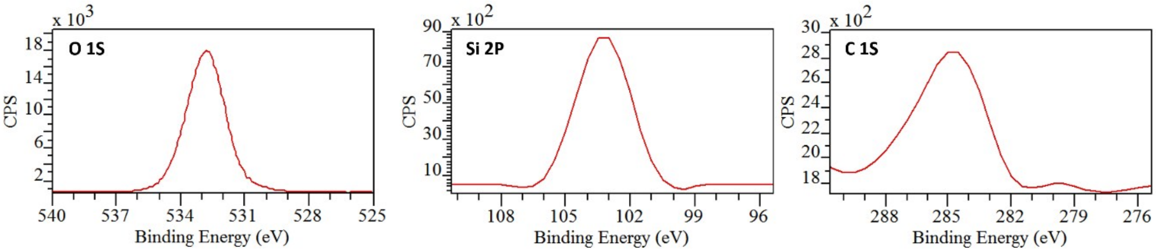

Fig. S8 X-ray photoelectron spectra of O 1S, Si 2P and C 1S of **1C**

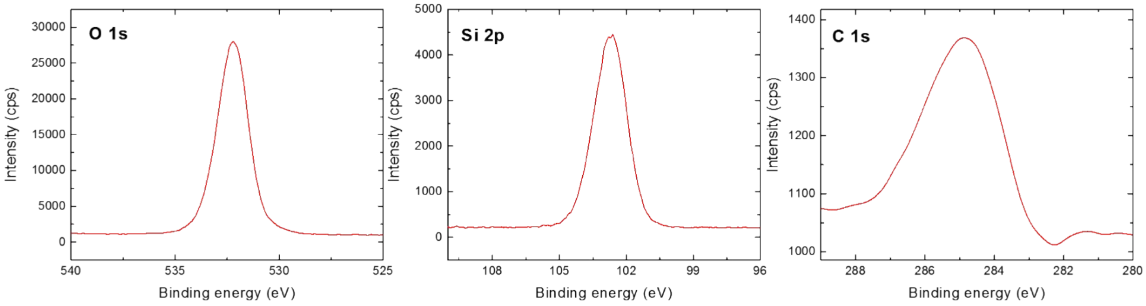

Fig. S9 X-ray photoelectron spectra of O 1S, Si 2P and C 1S of **2B**

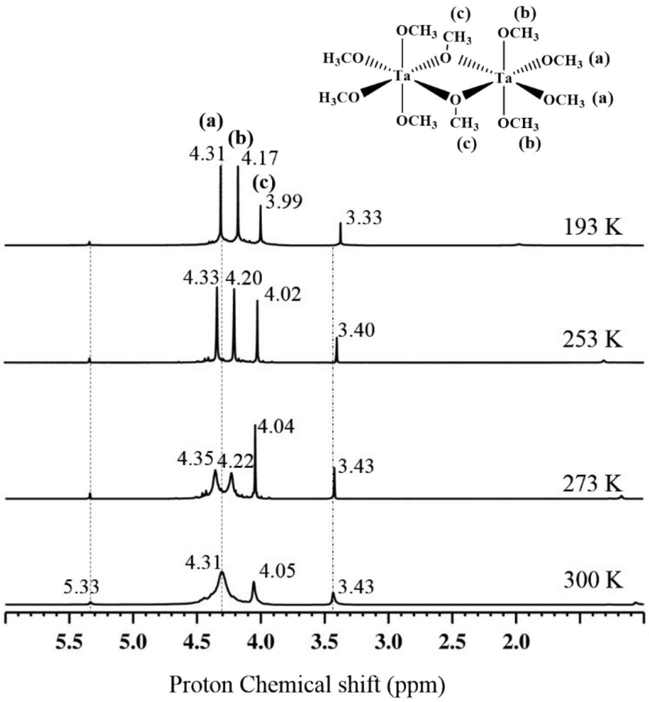

Fig. S10 One-dimensional (1 D) variable temperature liquid state ^{1}H NMR spectra of **2** in CD_2Cl_2.

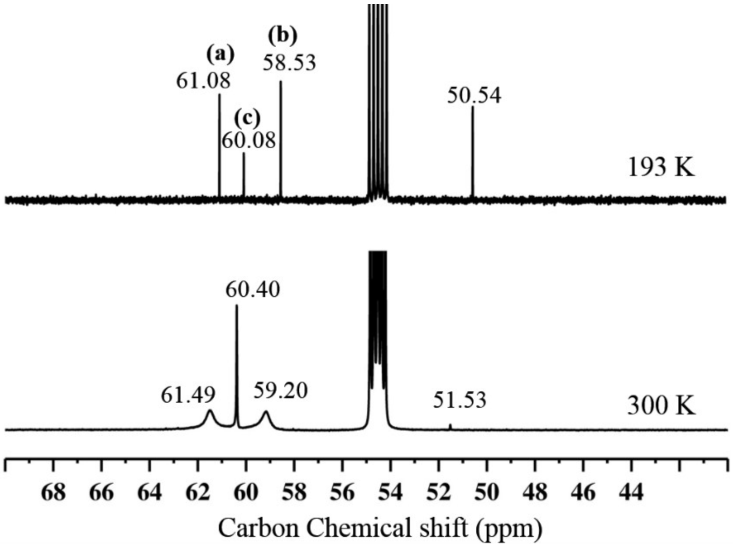

Fig. 11 One-dimensional (1 D) variable temperature liquid state ^{13}C NMR spectra of **2** in CD_2Cl_2.

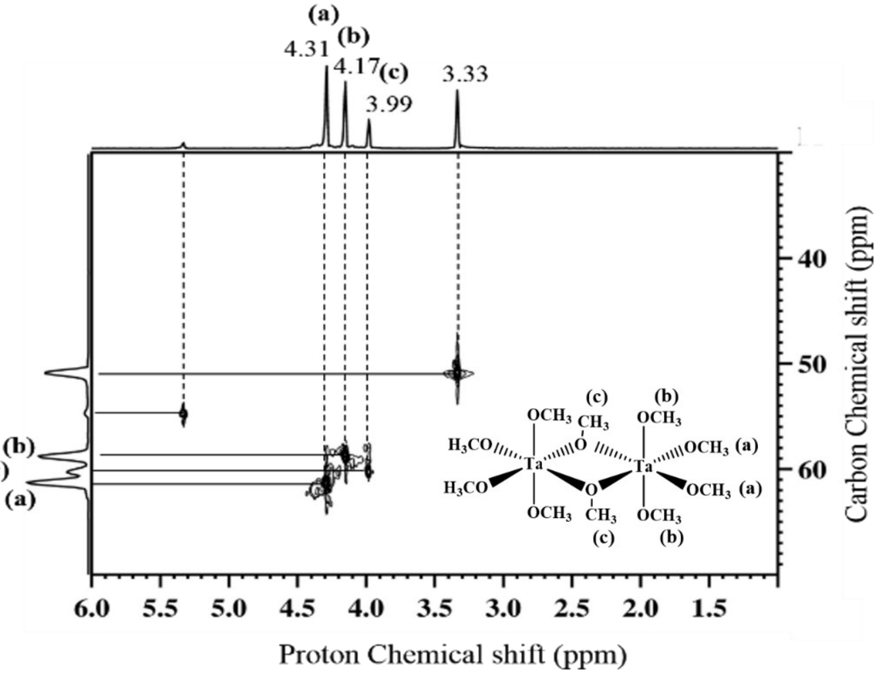

Fig. S12 Two-dimensional (2D) liquid-state ^{1}H-^{13}C Heteronuclear Single Quantum Correlation (HSQC) NMR spectrum of **2** in CD_2Cl_2 recorded at 196 K.

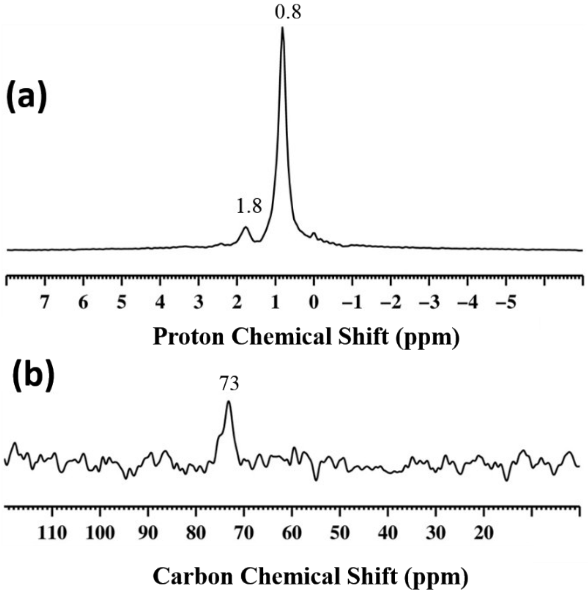

Fig. S13 (a) One-dimensional (1D) ^{1}H MAS NMR spectrum of **1A** acquired at 600 MHz with a 22 kHz MAS frequency, a repetition delay of 5 s, and 8 scans. (b) ^{13}C CP MAS NMR spectrum of **1A** (acquired at 400 MHz) with a 10 kHz MAS frequency, 10000 scans, a 4 s repetition delay, and a 2 ms contact time. Exponential line broadening of 80 Hz was applied prior to Fourier transformation. ^{13}C CP MAS spectra were acquired at its natural abundance.

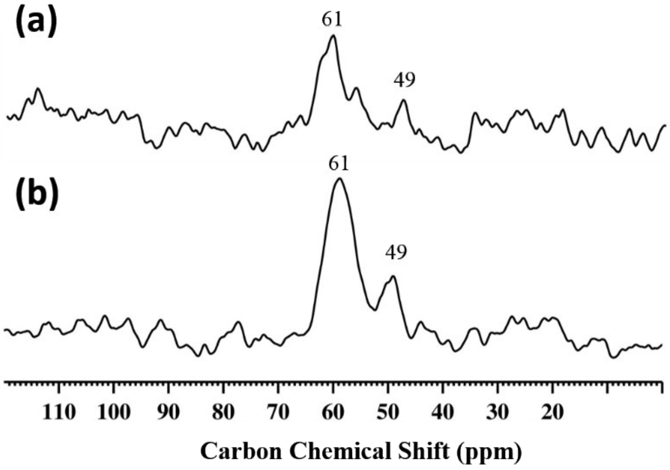

Fig. S14 ^{13}C CP/MAS NMR spectrum of (a) **1B** and (b) **2A** (acquired at 9.4 T) (^{1}H = 400 MHz) with a 10 kHz MAS frequency, 10000 scans, a 4 s repetition delay, and a 2 ms contact time. Exponential line broadening of 80 Hz was applied prior to Fourier transformation. ^{13}C CP/MAS spectra were acquired at its natural abundance.

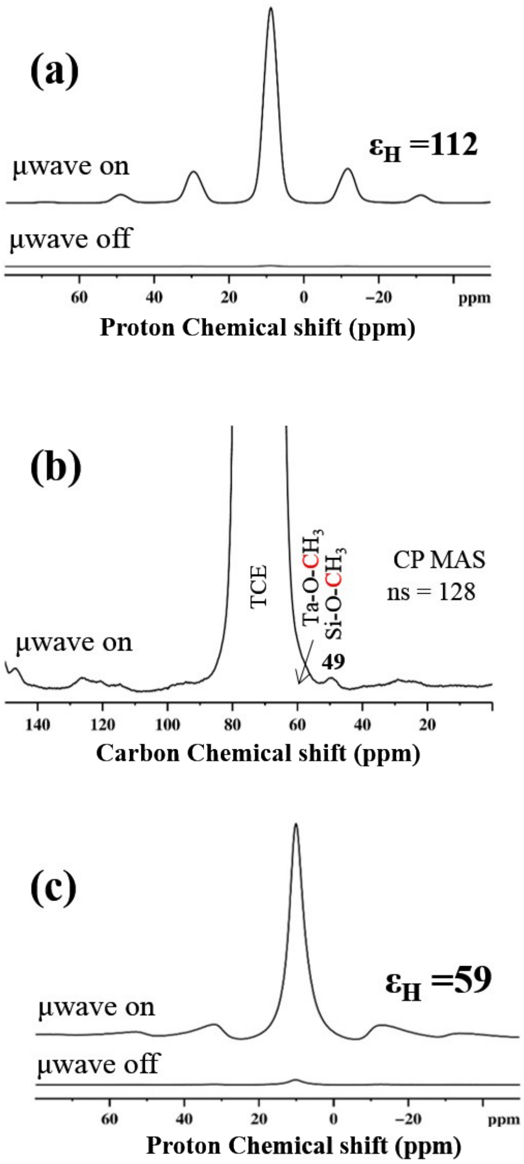

Fig. S15 (a) ^{1}H MAS DNP SENS spectra (100 K, 400 MHz /263 GHz gyrotron) of **1B** impregnated with 16 mM TEKPol in TCE solution acquired with 8 scans, recycle delay of 3 s and MAS frequency at 8 KHz. The spectra with and without µwave irradiation are labelled as µwave on and off. (b) ^{13}C CP MAS DNP SENS spectra(100 K, 400 MHz /263 GHzgyrotron) of **1B** impregnated with 16 mM TEKPol in TCE solution. The spectra were recorded using 128 scans under µwave irradiation, recycle delay of 3 s, contact time of 3 ms and MAS frequency at 8 KHz. (c) ^{1}H MAS DNP SENS spectra (100 K, 400 MHz / 263 GHz gyrotron)of **1B** impregnated with 16 mM of TEKPol in DCB solution acquired with 8 scans, recycle delay of 3 s and MAS frequency at 8 KHz.

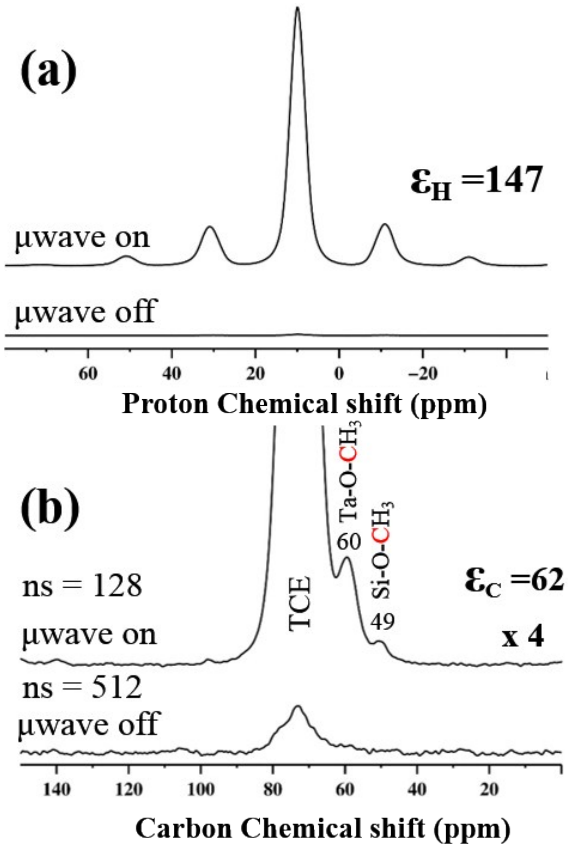

Fig. S16 (a) ^{1}H MAS DNP SENS spectra(100 K, 400 MHz /263 GHz gyrotron) of **2A** impregnated with 16 mM TEKPOL in TCE solution acquired with 8 scans, recycle delay of 3 s and MAS frequency at 8 KHz. The spectra with µwave irradiation on and off are given. (b) ^{13}C CP MAS DNP SENS spectra (100 K, 400 MHz / 263 GHz gyrotron) of **2A** impregnated with 16 mM TEKPOL in TCE solution. The spectra were recorded using 128 and 512 scans respectively for µwave irradiation on and off conditions; The recycle delay was 3 s, the contact time was 3 ms and the MAS frequency was 8 kHz.

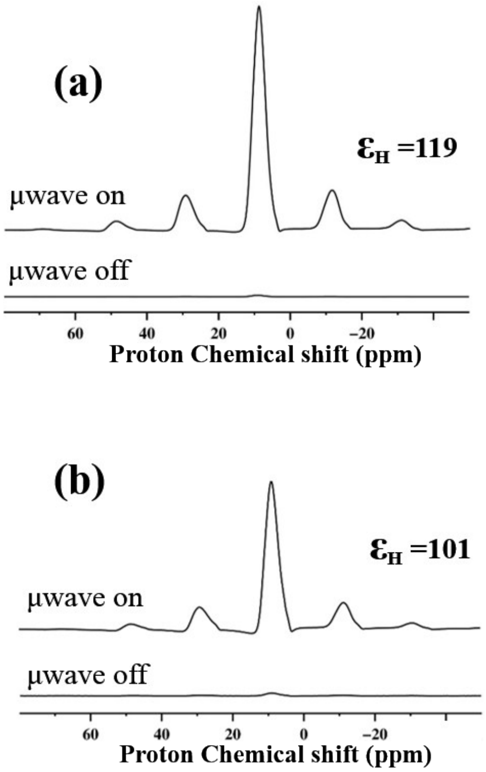

Fig. S17 ^{1}H MAS DNP SENS spectra (100 K, 400 MHz / 263 GHz gyrotron) of (a) **1C** and (b) **2B** impregnated with 16 mM TEKPol in TCE solution acquired with 8 scans, recycle delay of 3 s and MAS frequency at 8 KHz. The spectra with µwave irradiation on and off are given for both the spectra.

Table S4 (a) Catalytic activity results of as-synthesized $Ta_xN_y/TaO_xN_y/SiO_2$ for the cyclooctene epoxidation

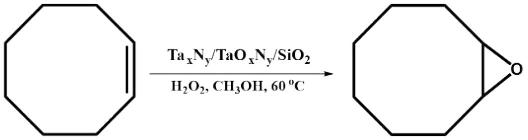

Catalyst	Ta - µmol (wt. %)	Epoxide Yield (%)	Conversion (%)	Selectivity (%)	TON
2B	1.0 (0.2)	20	24	99	1395
2B	4.5 (0.8)	41	48	98	639
2B	11.4 (2)	56	66	98	347
2B	**18.5 (3.4)**	**85**	**>99**	**97**	**>321**
1C	4.0 (0.7)	42	49	98	738
-*	N/A	7	9	98	N/A
SiO_2	N/A	8	10	87	N/A

*Reaction with H_2O_2 in the absence of catalyst; [Reaction conditions: 0.92 ml of cyclooctene; 4-70 mg of catalyst; 4.0 ml of methanol and 3.0 ml of H_2O_2 (30 wt. %); 333 K (60 °C) for 18 h]. Catalyst/olefin/H_2O_2 ratio used is in the order 1/10,000/100,000; TON= Epoxide(mols)/Ta(mol). Conversion values reported here are within ±2.3% error.

Table S4 (b) Catalytic activity results of as-synthesized $Ta_xN_y/TaO_xN_y/SiO_2$ (2B) for other substrate epoxidation

Catalyst	Substrate	Conversion (%)	Major products	Selectivity (%)
2B	Styrene	60	Benzaldehyde Styrene epoxide Phenyl acetaldehyde	21 61 18
2B	Cyclohexene	93	Cyclohexene oxide 2-Cyclohexen-1-one	99 <1
2B	1-Octene	94	1-Octene epoxide 1,2-Octanediol	96 <4

[Reaction conditions: Ta : (4.5 µmol; 0.8 wt.%), (styrene : 0.80 ml; of cyclohexene: 0.71 ml; 1-octene : 1 ml) 17 mg of catalyst used; 4.0 ml of methanol used as solvent and 1.0 ml of H_2O_2 as the oxidant (30 wt. %); 333 K (60 °C) for 18 h]. Catalyst/olefin/H_2O_2 ratio used is in the order 1/10,000/30,000; Conversion values reported here are within ±2% error.

Table S5 Catalytic activity results of various metal supported silica for the cyclooctene epoxidation (**From literature**[6])

Catalyst	Conversion (%)	Selectivity (%)
Zr-SiO_2[a]	8	36
Mn-SiO_2[a]	5	81
Ti-SiO_2[a]	10	88
V-SiO_2[a]	35	73
Cr-SiO_2[a]	43	76
Mo(acac)-SiO_2[a]	57	95
⊗Ta/SBA-15[a]	65	43
Nb/MCM-41[c]	50	>99

[a] 1 wt% metal in the catalyst; [c] 1.8 wt% metal in the catalyst

Different types of metal precursors were used; TBHP was used as the oxidant

Reaction conditions: 10 mmol cyclooctene, 7 mmol TBHP (47.9% in EtOAc), 2.5 mmol n-decane and 25 mg of catalyst; 333 K; 24 h.

⊗Reaction conditions: cyclooctene 2.0 mmol, H_2O_2 4.0 mmol, CH_3CN 2.0 ml, catalyst 25 mg, 335 K, 24 h.

---

[6] (a) U. Arnold, R. Serpa da Cruz, D. Mandelli and U. Schuchardt, *J. Mol. Catal. A: Chem.*, 2001, **165**, 149-158.
(b) M.-L. Lin, K. Hara, Y. Okubo, M. Yanagi, H. Nambu and A. Fukuoka, *Catal. Commun.*, 2011, **12**, 1228-1230.

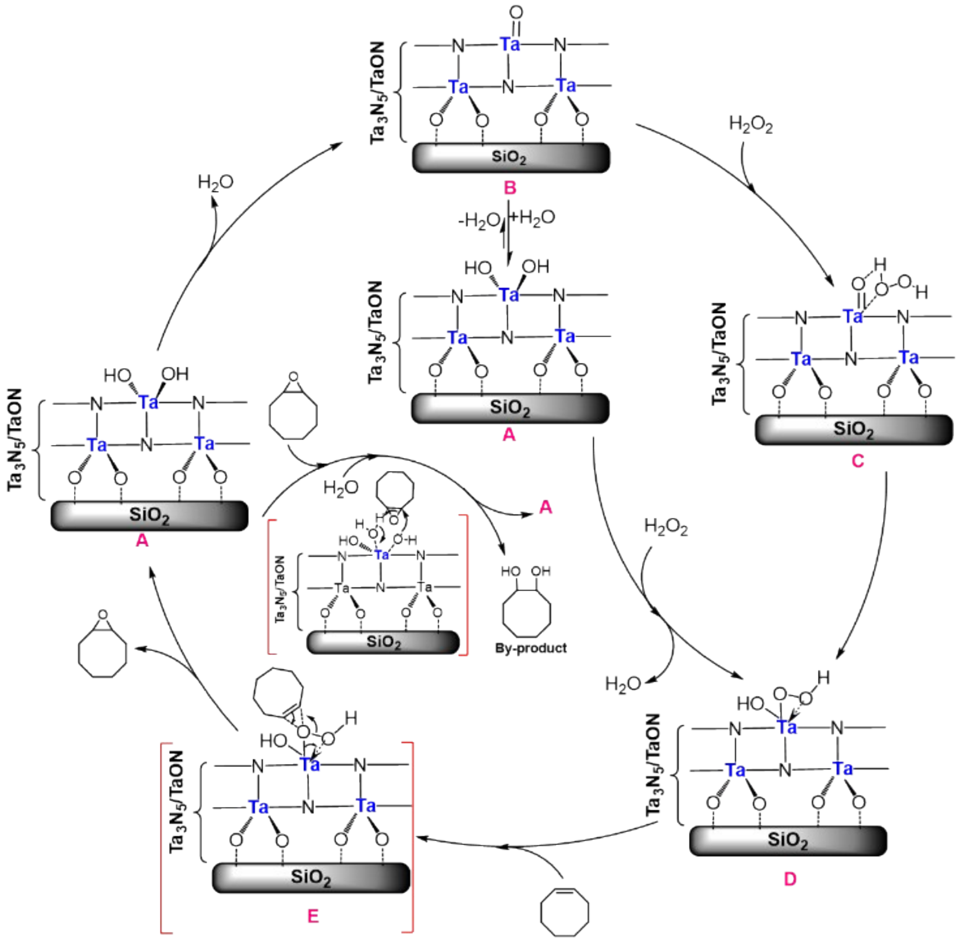

Scheme S3 A tentative mechanistic pathway for the cyclooctene epoxidation catalysed by Ta_xN_y/TaO_xN_y NPs on SiO_2 surface. [This scheme does not consider the surface inhomogenities and is purely based on the general known mechanism].

The actual mechanism is always a question of debate. There are two possibilities. They are based on the fact that the peroxo intermediate might induce activity by either O transfer to an alkene doing epoxidation or by homolytic scission of peroxo O-O bond resulting in the allylic oxidation of the alkene by a radical mechanism. As epoxide is formed selectively, we assume that the former mechanism might be operating here. A schematic representation of the anticipated active site is provided in this scheme. Surface inhomogeneity was not considered while suggesting the tentative pathway. The active site could be a surface N_x-Ta=O or N_x-Ta-$(OH)_2$ as shown in **A** and **B**.

Upon reaction with H_2O_2, either of this species generate $[N_x(O_y)Ta(OH)\text{-}O\text{-}O\text{-}H]^*$ (**D**) which could be responsible for the partial oxidation of the cyclic alkene. When cyclooctene is introduced into the reaction mixture, an intermediate (**E**) could be formed which facilitate the oxygen abstraction from the metal peroxo complex by virtue of the instability of the partially formed metal peroxo tricyclic ring and thus releasing the cyclooctene epoxide. The oxidant used is 30 wt. % H_2O_2 solution in water and hence, it is probable that the highly basic sites as shown in (**A**) may also catalyze the hydrolysis of the cyclooctene epoxide formed to yield cyclooctene diol as the by-product. As the selectivity obtained under the reaction conditions is ~98%, such a side reaction is considered to be minimum. The active site **A** or **B** could be regenerated at the end of the cycle as shown in scheme 3. A similar mechanism has been proved in the case of different active sites in different substrates epoxidation reactions.

Details of EXAFS Fitting

Sample 1A

Three EXAFS scans were recorded in order to reduce the error. However, the spectra show that the sample underwent stoichiometric changes when being scanned, as indicated by the isosbestic points in the spectra (Figures S18). Therefore, only the first scan was used for analysis.

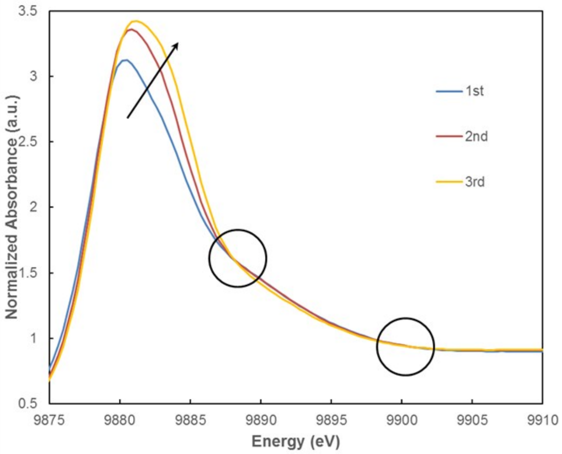

Figure S18. XANES region of XAS at Ta L_3 edge characterizing Ta complex **1A** formed by supporting $TaMe_5$ on SiO_2-700. The isosbestic points marked by circles show that the sample underwent a stoichiometric change during the scan.

The first attempt was made on a postulated model [(Si–O)–Ta–$(CH_3)_4$] (Model I in Table S6). Three shells, Ta–C_{methyl}, Ta–$O_{support}$, and Ta–$Si_{support}$, were fitted in the model, giving a goodness of fit of 6.32. The model was rejected because the Deby-Waller factor ($\Delta\sigma^2$) in the Ta–$Si_{support}$ is too small in comparison with the values in previous reports[7]. A simplified model, Model II, with only Ta–C_{methyl} and Ta–$O_{support}$ shells, was built with an expense of slightly increased goodness of fit. The absorber-backscatterer distances (*R*) of the shells are within the reasonable range, and the coordination numbers (*N*) consistent with the expectation that the sample predominantly consisted of a monopodal species, [(SiO)–Ta–$(CH_3)_4$]. with a small amount of a bipodal species, [$(SiO)_2$–Ta–$(CH_3)_3$]. The bipodal species may be formed by an X-ray-induced conversion, as also seen in the SiO_2-supported pentamethyl tungsten[8]. The comparison of data with fitted models, Model I and II, in overall *k*-range, *R*-range, as well as the individual shells, were shown in Figure S19 and S20, respectively.

---

[7] (a) Taoufik, M.; De Mallamann, A.; Prouzet, E.; Saggio, G.; Thivolle-Cazat, J.; Basset, J. M. *Organometallics* 2001, **20**, 5518. (b) Saggio, G.; De Mallmann, A.; Maunders, B.; Taoufik, M.; Thivolle-Cazat, J.; Basset, J. M. *Organometallics* 2002, **21**, 5167. (c) Rataboul, F.; Chabanas, M.; De Mallmann, A.; Copéret, C.; Thivolle-Cazat, J.; Basset, J. M. Chem. - A Eur. J. 2003, **9**, 1426.

[8] Maity, N.; Barman, S.; Callens, E.; Samantaray, M. K.; Abou-Hamad, E.; Minenkov, Y.; D'Elia, V.; Hoffman, A. S.; Widdifield, C. M.; Cavallo, L.; Gates, B. C.; Basset, J.-M. *Chem. Sci.* 2016, **7**, 1558.

Table S6: Summary of EXAFS fit parameters[a] characterizing Ta complex **1A** formed by supporting $TaMe_5$ on SiO_2-700. EXAFS data were collected at 77 K with sample under vacuum.

Model	Shell	*N*	*R* (Å)	*Δσ*^{2} × 10^3 (Å^2)	*ΔE$_0$* (eV)	*k*-range (Å^{-1})	*R*-range (Å)	*Goodness of fit*
I[b]	Ta–C_{methyl}					3.37 – 9.95	0.5 – 3.0	6.32
	Ta–$O_{support}$	1.7	1.90	1.9	-8.3			
	Ta–$Si_{support}$	1.2	3.31	0.5	5.4			
II[c]	Ta–C_{methyl}	4.0	2.20	3.0	-10.0	3.37 – 9.95	0.5 – 2.4	6.40
	Ta–$O_{support}$	1.5	1.90	1.0	-9.7			

[a] Notation: *N*, coordination number; *R*, absorber-backscatterer distance; $\Delta\sigma^2$, disorder term (Debye-Waller factor); ΔE_0, inner potential correction. The number of statistically free parameters determined using the Nyquist theorem is 12 and 9 for Model I and II, respectively. Estimated error bounds for each parameter are as follows: *N* ±20%; *R* ±0.02 Å; $\Delta\sigma^2$ ±20%; ΔE_0 ±20%. [b] $\Delta\sigma^2$ value in Ta–$Si_{support}$ shell is too small. [c] Recommended model.

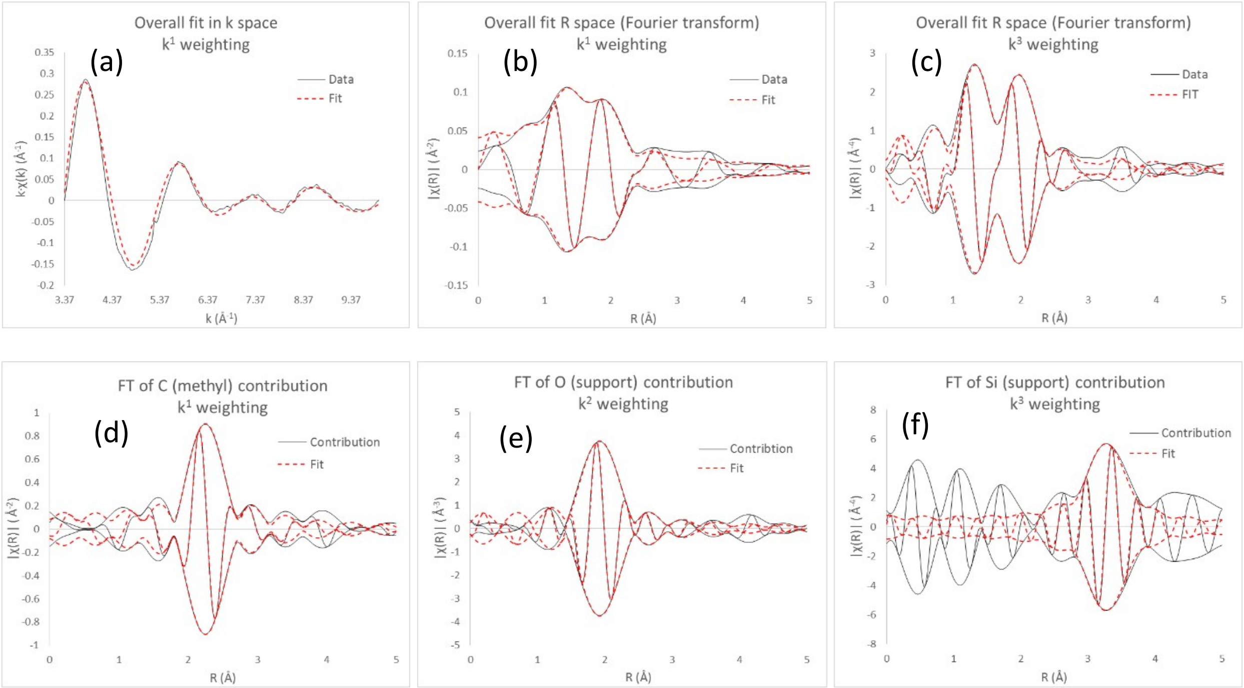

Figure S19. Fitted model I for EXAFS data characterizing tantalum complex formed by supporting $TaMe_5$ on SiO_2-700. (a) k^1-weighted EXAFS function and overall fit; (b) k^1-weighted Fourier transform of the EXAFS function and overall fit; (c) k^3-weighted Fourier transform of the EXAFS function and overall fit; (d) k^1-weighted Fourier transform of residual data and modeled contribution of the Ta–C_{methyl} shell; (e) k^2-weighted Fourier transform of residual data and modeled contribution of the Ta–$O_{support}$ shell; (f) k^3-weighted Fourier transform of residual data and modeled contribution of the Ta–$Si_{support}$ shell.

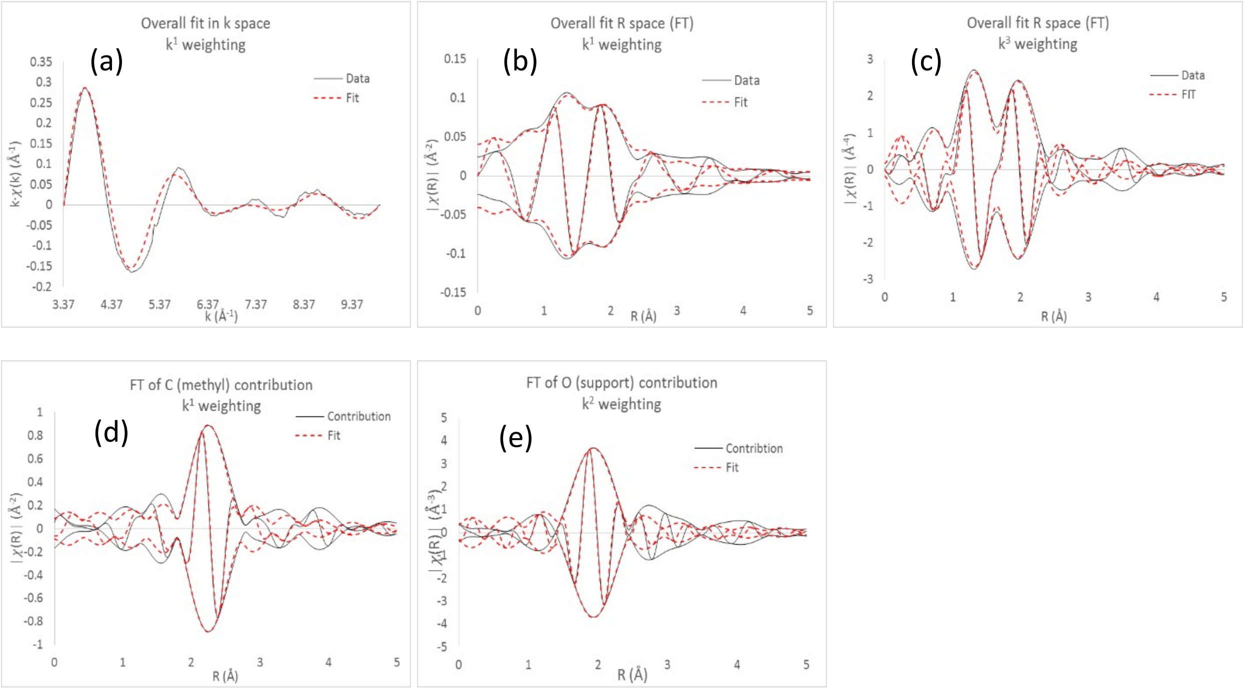

Figure S20. Fitted model II for EXAFS data characterizing Ta complex formed by supporting $TaMe_5$ on SiO_2-700. (a) k^1-weighted EXAFS function and overall fit; (b) k^1-weighted Fourier transform of the EXAFS function and overall fit; (c) k^3-weighted Fourier transform of the EXAFS function and overall fit; (d) k^1-weighted Fourier transform of residual data and modeled contribution of the Ta–C_{methyl} shell; (e) k^2-weighted Fourier transform of residual data and modeled contribution of the Ta–$O_{support}$ shell.

Sample 1B

Three EXAFS scans were recorded, with high consistency in the spectra, and were averaged for analysis.

In fitting the data characterizing **1B**, we began with a model incorporating methoxy groups and support O atoms bonded to the Ta, so that there were three shells, two Ta–O shells and one Ta–C shell. We did not find a satisfactory fit and were not able to resolve O in the support and O in the methoxy groups. Thus, we made a simplifying assumption that the two Ta–O contributions could be represented by one shell. Three models were fitted based upon such assumption, as listed in Table S7.

Model I and II consist four shells: (1) a Ta–O contribution (where O represents unresolved methoxy and support O atoms), (2) a Ta–C contribution, (3) another a Ta–O contribution to represent the interaction of Ta with O atoms of the support at a distance greater than a bonding distance, and (4) another Ta–light atom contribution. In Model I, the light atom is C; in Model II, it is O. These models provided satisfactory fits, with Model II giving a slightly better fit. However, the coordination number of the Ta–$O_{methoxy/support}$ shell is lower than the expected ratio, which is ~5 suggested by the elemental analysis. This might be caused by the X-ray damage on the sample with the release of methanol from the methoxy groups. On the other hand, the coordination number of the Ta–$C_{methoxy}$ shell, which is expected to match the number of oxygens, is greater than the latter. Note that the interaction between the tantalum center and the silicon atom from the SiO_2 support was not resolved in both of the models. A possible Ta–$Si_{support}$ contribution might be buried in the Ta–$C_{methoxy}$ shell, thus the coordination number of the shell reflects the total number of the carbon and silicon atoms. Thus, these two models, though providing the clues for the possible structures of the sample, are less than quantitative, reflecting the limitations of EXAFS spectroscopy for structures.

Model III is a simplified model derived from removing the long Ta–O shell in Model II. The goodness of fit of the model is too high to be considered as a satisfactory fit, thus was rejected.

The comparison of data with fitted models, Model I, II, and III, in overall *k*-range, *R*-range, as well as the individual shells, were shown in Figure S21, S22, and S23, respectively.

Table S7: Summary of EXAFS fit parameters[a] characterizing Ta complex **1B** formed by supporting $TaMe_5$ on SiO_2-700 and treating in flowing O_2 at RT. EXAFS data wercollected at 77 K under vacuum.

Model	Shell	*N*	*R* (Å)	$\Delta\sigma^2 \times 10^3$ (Å^2)	ΔE_0 (eV)	*k*-range (Å^{-1})	*R*-range (Å)	*Goodness of fit*
I[b]	Ta–$O_{methoxy/support}$	2.0	1.86	3.7	3.2	3.41 – 10.75	0.5 – 4.0	6.19
	Ta–C[c]	2.3	2.57	1.1	14.4			
	Ta–$C_{methoxy}$[d]	3.5	3.18	6.2	-14.7			
	Ta–O_{long}[e]	5.2	3.76	10.4	-6.6			
II[b]	Ta–$O_{methoxy/support}$	2.0	1.85	3.6	4.6	3.41 – 10.75	0.5 – 4.0	5.30
	Ta–O[c]	1.6	2.55	1.4	7.5			
	Ta–$C_{methoxy}$[d]	4.2	3.20	8.2	-14.7			
	Ta–O_{long}[e]	3.7	3.75	6.4	-5.8			
III[f]	Ta–$O_{methoxy/support}$	2.0	1.86	3.7	3.2	3.41 – 10.75	0.5 – 3.0	36.09
	Ta–O[c]	1.5	2.54	1.1	7.2			
	Ta–$C_{methoxy}$[d]	5.0	3.16	9.0	-12.3			

[a] Notation: *N*, coordination number; *R*, absorber-backscatter distance; $\Delta\sigma^2$, disorder term (Debye-Waller factor); ΔE_0, inner potential correction. The number of statistically free parameters determined using the Nyquist theorem is 16, 16, and 18, 18, and 13 for Model I, II, and III, respectively. Estimated error bounds for each parameter are as follows: *N* ±20%; *R* ±0.02 Å; $\Delta\sigma^2$ ±20%; ΔE_0 ±20%. [b] Either of the models cannot be rejected due to the similar values of *Goodness of fit*. [c] Shells correspond to the peak at ~2.0 Å in R-space. [d] May contains a Ta–Si contribution that was not separated from the shell. [e] Long contribution from oxygen of SiO_2 support. [f] *Goodness of fit* is too high.

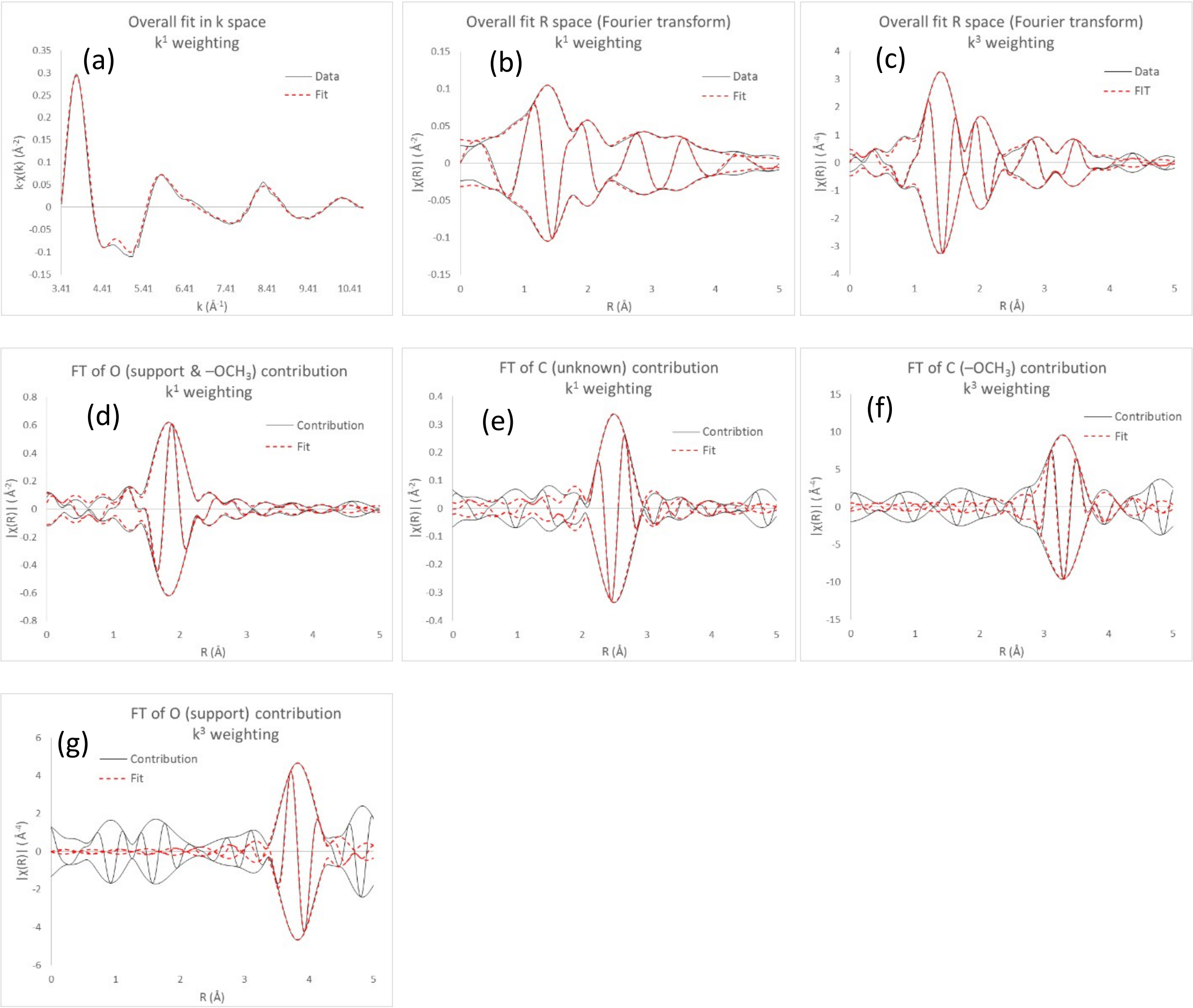

Figure S21. Fitted model I for EXAFS data characterizing Ta complex **1B** formed by supporting $TaMe_5$ on SiO_2-700 and treating the sample in flowing O_2 at room temperature. (a) k^1-Weighted EXAFS function and overall fit; (b) k^1-weighted Fourier transform of the EXAFS function and overall fit; (c) k^3-weighted Fourier transform of the EXAFS function and overall fit; (d) k^1-weighted Fourier transform of residual data and modeled contribution of the Ta–$O_{methoxy/support}$ shell; (e) k^1-weighted Fourier transform of residual data and modeled contribution of the Ta–C shell; (f) k^3-weighted Fourier transform of residual data and modeled contribution of the Ta–$C_{methoxy}$ shell; (g) k^3-weighted Fourier transform of residual data and modeled contribution of the Ta–$O_{support}$ shell.

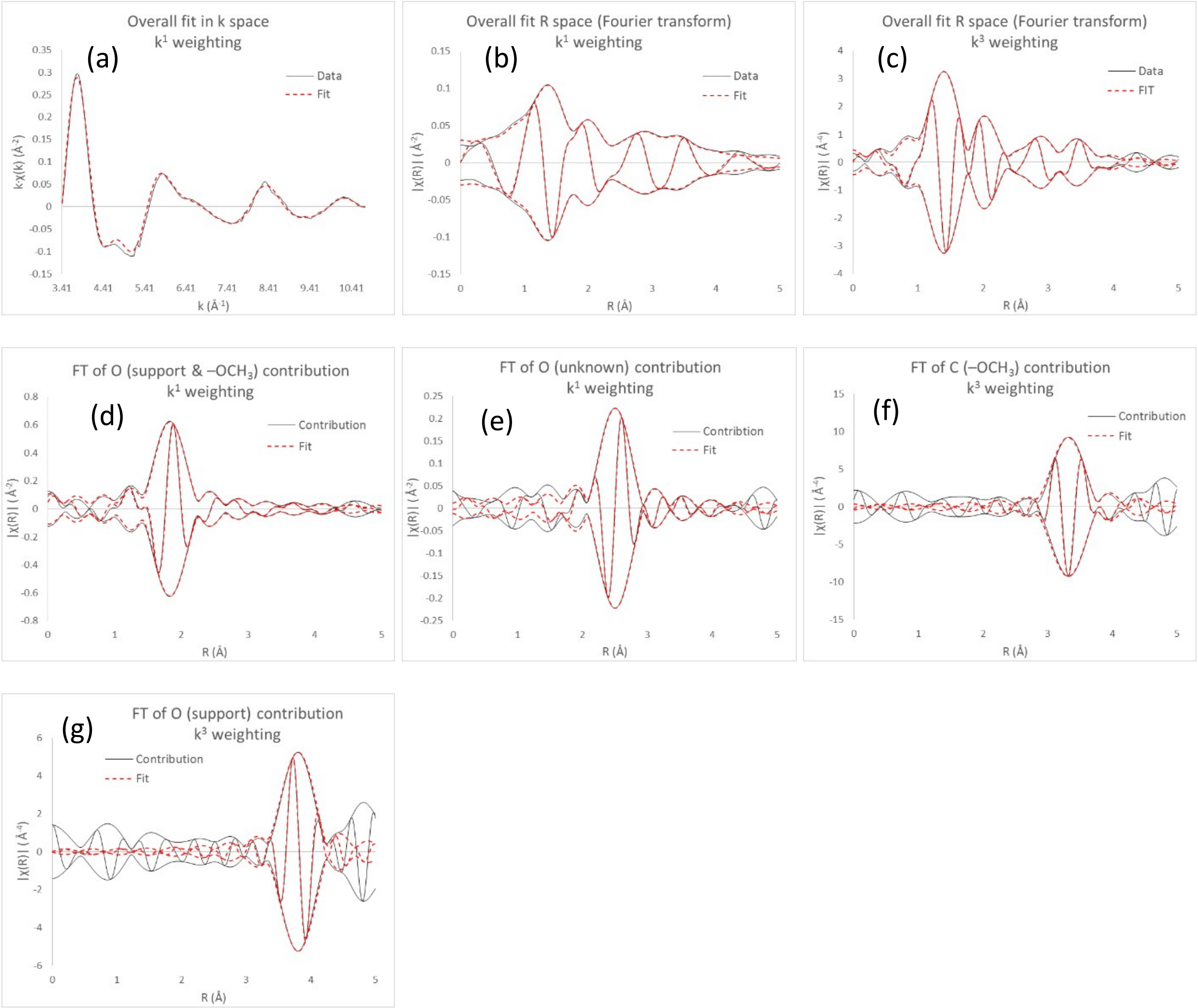

Figure S22. Fitted model II for EXAFS data characterizing Ta complex **1B** formed by supporting $TaMe_5$ on SiO_2-700 and treating in O_2 flow at RT. (a) k^1-weighted EXAFS function and overall fit; (b) k^1-weighted Fourier transform of the EXAFS function and overall fit; (c) k^3-weighted Fourier transform of the EXAFS function and overall fit; (d) k^1-weighted Fourier transform of residual data and modeled contribution of the Ta–$O_{methoxy/support}$ shell; (e) k^1-weighted Fourier transform of residual data and modeled contribution of the Ta–O shell; (f) k^3-weighted Fourier transform of residual data and modeled contribution of the Ta–$C_{methoxy}$ shell; (g) k^3-weighted Fourier transform of residual data and modeled contribution of the Ta–$O_{support}$ shell.

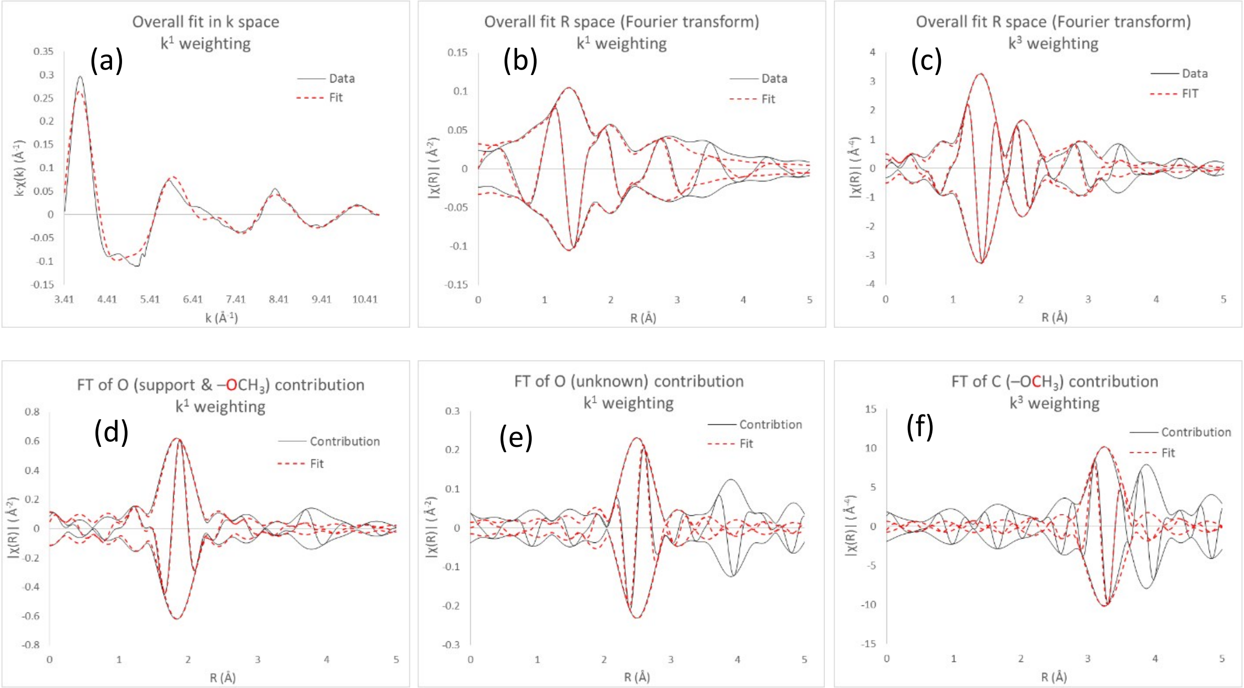

Figure S23. Fitted model III for EXAFS data characterizing Ta complex **1B** formed by supporting $TaMe_5$ on SiO_2-700 and treating in O_2 flow at RT. (a) k^1-weighted EXAFS function and overall fit; (b) k^1-weighted Fourier transform of the EXAFS function and overall fit; (c) k^3-weighted Fourier transform of the EXAFS function and overall fit; (d) k^1-weighted Fourier transform of residual data and modeled contribution of the Ta–$O_{methoxy/support}$ shell; (e) k^1-weighted Fourier transform of residual data and modeled contribution of the Ta–O shell; (f) k^3-weighted Fourier transform of residual data and modeled contribution of the Ta–$C_{methoxy}$ shell.

Sample 2

Three EXAFS scans were recorded in order to reduce the error. However, the spectra exhibit an unexpected change during the first scan, suggesting a shifting of the sample in the cell; in the second scan, the intensity declined as a function of time. In contrast, the third scan was stable (Figure S24). Thus, only the third scan was used for analysis.

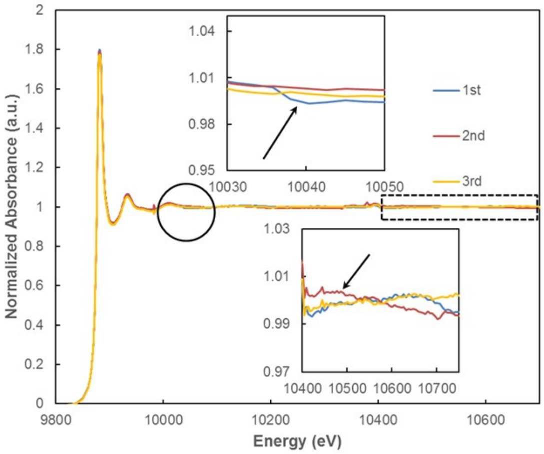

Figure S24. XAS at Ta L_3 edge characterizing tantalum complex **2** formed by supporting $Ta_2(OMe)_{10}$ on SiO_2-700. The insets show the spectra enlarged in the specific regions indicating the unexpected change during the first scan and the declination in the second.

The models for EXAFS data characterizing the dimeric precursor **2**, for which there is no known crystal structure, were listed in Table S8. The recommended model, Model I, demonstrates a Ta–Ta contribution, with a coordination number of 1 (with error) at a distance of 3.34 Å, consistent with a dimer. The model also give evidence of methoxy groups, but the Ta–O and Ta–C coordination numbers were about 3, rather than the value of 5 expected on the basis of $Ta(OMe)_5$ concentration. Thus, the data are less than sufficient for a structure determination. We postulate that the sample was degraded under the influence of the X-ray beam in the experiment, consistent with our observation that the second and third scans were different from the first (Figure S24).

Model II was built by removing the Ta–Ta contribution from Model I, assuming that the sample is not a dimer. The fit results in an inappropriate absorber-backscatterer distance (R = 3.67 Å) of the Ta–$C_{methoxy}$ contribution, larger than a possible bonding distance of Ta–$C_{methoxy}$. Thus the model was rejected.

The comparison of data with fitted models, Model I and II, in overall *k*-range, *R*-range, as well as the individual shells, were shown in Figure S25 and S26, respectively.

Table S8: Summary of EXAFS fit parameters[a] characterizing $Ta_2(OMe)_{10}$ (**2**). EXAFS data were collected at 77 K under vacuum.

Model	Shell	*N*	*R* (Å)	$\Delta\sigma^2 \times 10^3$ (Å^2)	ΔE_0 (eV)	*k*-range (Å^{-1})	*R*-range (Å)	*Goodness of fit*
I[b]	Ta–$O_{t\text{-methoxy}}$	2.0	1.88	4.7	3.8	3.41 – 9.99	0.5 – 4.0	5.00
	Ta–$O_{b\text{-methoxy}}$	2.0	2.20	3.4	-2.7			
	Ta–C_{methoxy}	4.0	3.15	9.9	-13.6			
	Ta–Ta	1.2	3.40	4.5	-11.2			
II[c]	Ta–$O_{t\text{-methoxy}}$	2.0	1.88	4.7	3.8	3.41 – 9.99	0.5 – 4.0	6.52
	Ta–$O_{b\text{-methoxy}}$	2.0	2.20	3.4	-2.7			
	Ta–C_{methoxy}	8.2	3.67	10.3	-1.5			

[a] Notation: *N*, coordination number; *R*, absorber-backscatterer distance; $\Delta\sigma^2$, disorder term (Debye-Waller factor); ΔE_0, inner potential correction. The number of statistically free parameters determined by using the Nyquist theorem is 16 for each model. Estimated error bounds for each parameter are as follows: *N* ±20%; *R* ±0.02 Å; $\Delta\sigma^2$ ±20%; ΔE_0 ±20%. [b] Recommended model. [c] Inappropriate values of *N* and *R* in Ta–C_{methyl} shell.

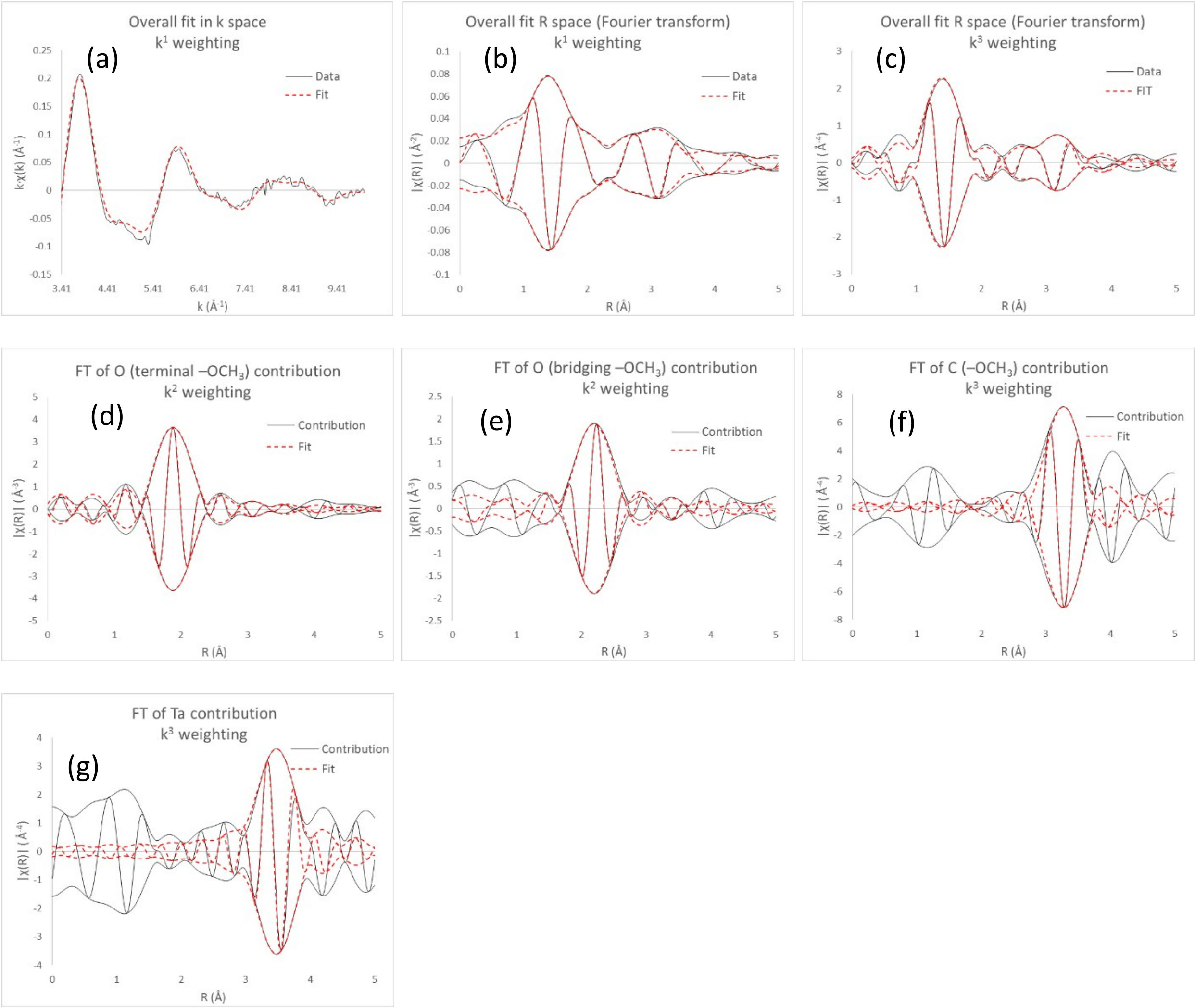

Figure S25. Fitted model I for EXAFS data characterizing $Ta_2(OMe)_{10}$ (**2**) under vacuum at 77 K. (a) k^1-weighted EXAFS function and overall fit; (b) k^1-weighted Fourier transform of the EXAFS function and overall fit; (c) k^3-weighted Fourier transform of the EXAFS function and overall fit; (d) k^2-weighted Fourier transform of residual data and modeled contribution of the Ta–$O_{t\text{-methoxy}}$ shell; (e) k^2-weighted Fourier transform of residual data and modeled contribution of the Ta–$O_{b\text{-methoxy}}$ shell; (f) k^3-weighted Fourier transform of residual data and modeled contribution of the Ta–C_{methoxy} shell; (g) k^3-weighted Fourier transform of residual data and modeled contribution of the Ta–Ta shell.

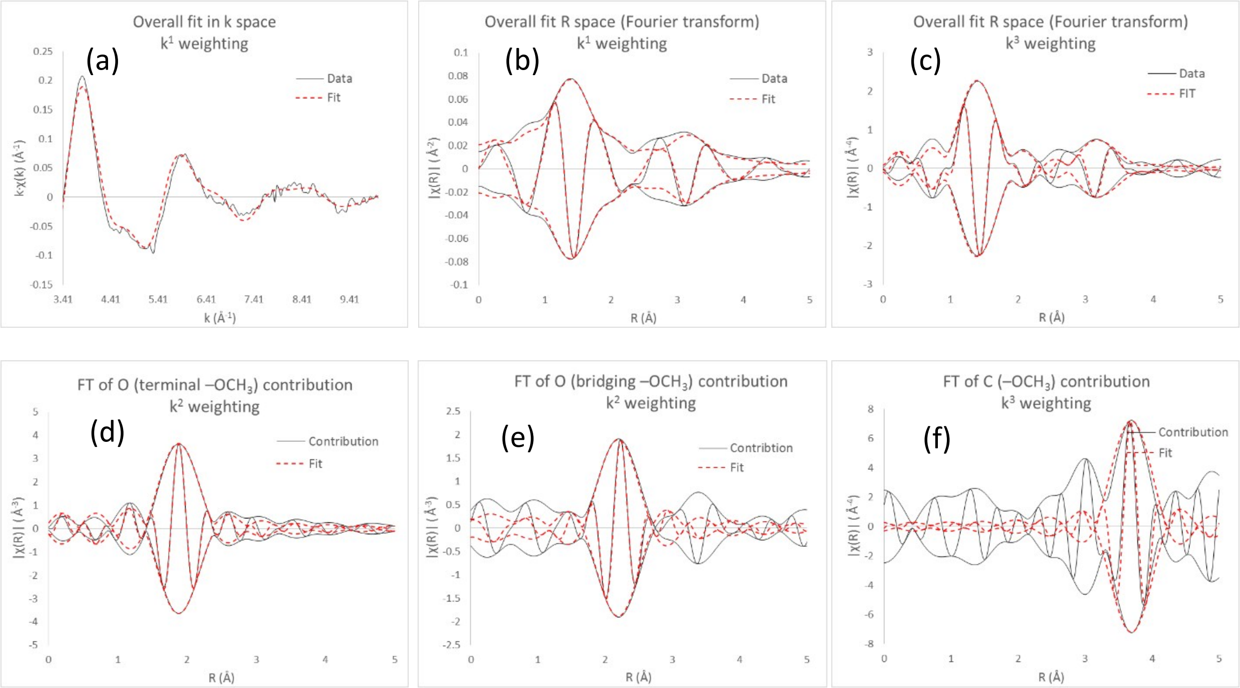

Figure S26. Fitted model II for EXAFS data characterizing $Ta_2(OMe)_{10}$ (**2**) under vacuum at 77 K. (a) k^1-weighted EXAFS function and overall fit; (b) k^1-weighted Fourier transform of the EXAFS function and overall fit; (c) k^3-weighted Fourier transform of the EXAFS function and overall fit; (d) k^2-weighted Fourier transform of residual data and modeled contribution of the Ta–$O_{t\text{-methoxy}}$ shell; (e) k^2-weighted Fourier transform of residual data and modeled contribution of the Ta–$O_{b\text{-methoxy}}$ shell; (f) k^3-weighted Fourier transform of residual data and modeled contribution of the Ta–C_{methoxy} shell.

Sample 2A

Three EXAFS scans were recorded in order to reduce the error. However, the spectra show that the sample underwent stoichiometric changes when being scanned, as indicated by the isosbestic points in the spectra (Figures S27). Therefore, only the first scan was used for analysis.

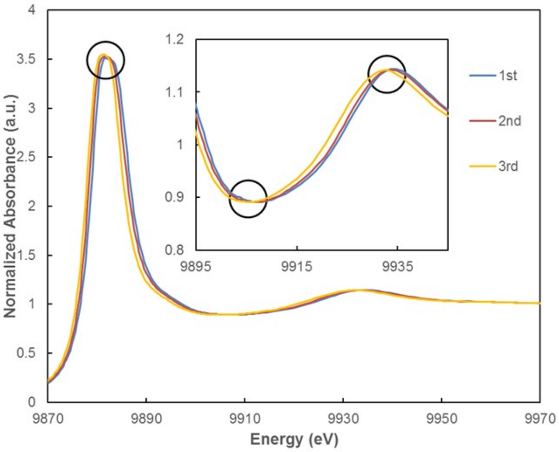

Figure S27. XANES region of XAS at Ta L_3 edge characterizing tantalum complex **2A** formed by supporting $Ta_2(OMe)_{10}$ on SiO_2-700. The isosbestic points marked by circles show that the sample underwent a stoichiometric change during the scan.

The same simplification to combine oxygen contributions of the methoxy groups and support oxygen, as was made in the analysis of sample **1B**, was also applied in sample **2A**, due to the limited resolution to justify the various Ta–O contributions**.** Model I was built based on the expected structure, with three shells: (1) a Ta–O contribution where O represents unresolved methoxy and support O atoms, (2) a Ta–C contribution where C presents the interaction of Ta with C atoms of the methoxy groups, (3) a Ta–Si contribution where Si is from the SiO_2 support. The fit leads to a goodness of fit too high to be considered as a satisfactory fit. In order to improve the fit, two new models were considered. In model II, a Ta–Ta contribution was added considering the possibility that the dimeric precursor failed to break into single-site. The model gave the lowest goodness of fit among the models listed in Table S9. However, the absorber-backscatterer distance of $Ta–Si_{support}$ shell is shell is out of the appropriate range, 3.2–3.4 Å, as reported in the literature[9]. Thus, the model was rejected. In model III, another a Ta–O contribution was added, which represents the interaction of Ta with O atoms of the support at a distance greater than a bonding distance. The model, though has a slightly larger goodness of fit than Model I does, gives all the parameters in the appropriate ranges, except for the coordination number of the $Ta–O_{methoxy/support}$ shell, which is less than the expected value of 5. This may be caused by an X-ray-induced sample damage, as we confirmed in XANES spectra (Figure S27) the sample underwent a stoichiometric change when it was scanned. The lack of Ta–Ta contribution supports the inference that the dimeric precursor broke and single-site species formed successfully.

The comparison of data with fitted models, Model I, II, and III, in overall *k*-range, *R*-range, as well as the individual shells, were shown in Figure S28, S29, and S30, respectively.

---

[9] (a) Taoufik, M.; De Mallamann, A.; Prouzet, E.; Saggio, G.; Thivolle-Cazat, J.; Basset, J. M. *Organometallics* 2001, **20**, 5518. (b) Saggio, G.; De Mallmann, A.; Maunders, B.; Taoufik, M.; Thivolle-Cazat, J.; Basset, J. M. *Organometallics* 2002, **21**, 5167. (c) Rataboul, F.; Chabanas, M.; De Mallmann, A.; Copéret, C.; Thivolle-Cazat, J.; Basset, J. M. Chem. - A Eur. J. 2003, **9**, 1426.

Table S9: Summary of EXAFS fit parameters[a] characterizing Ta complex **2A** formed by supporting $Ta_2(OMe)_{10}$ on SiO_2-700. EXAFS data were collected at 77 K under vacuum.

Model	Shell	*N*	*R* (Å)	$\Delta\sigma^2 \times 10^3$ (Å^2)	ΔE_0 (eV)	*k*-range (Å^{-1})	*R*-range (Å)	*Goodness of fit*
I	Ta–O$_{\text{methoxy/support}}$	3.4	1.88	6.3	2.0	3.42 – 9.81	0.5 – 3.5	43.04
	Ta–C$_{\text{methoxy}}$	3.3	3.18	0.2	-16.1			
	Ta–Si$_{\text{support}}$	1.9	3.50	7.1	-7.6			
II[b]	Ta–O$_{\text{methoxy/support}}$	3.3	1.88	6.2	2.3	3.42 – 9.81	0.5 – 4.0	19.19
	Ta–C$_{\text{methoxy}}$	3.3	3.19	0.1	-17.6			
	Ta–Ta	1.2	3.34	1.1	-12.0			
	Ta–Si$_{\text{support}}$	2.5	3.63	3.5	-12.6			
III[c]	Ta–O$_{\text{methoxy/support}}$	3.3	1.88	6.3	1.5	3.42 – 9.81	0.5 – 4.0	24.24
	Ta–C$_{\text{methoxy}}$	3.3	3.11	0.1	-16.6			
	Ta–Si$_{\text{support}}$	2.8	3.33	5.2	3.7			
	Ta–O$_{\text{long}}$[d]	5.8	3.78	10.9	-8.3			

[a] Notation: *N*, coordination number; *R*, absorber-backscatter distance; $\Delta\sigma^2$, disorder term (Debye-Waller factor); ΔE_0, inner potential correction. The number of statistically free parameters determined using the Nyquist theorem is 14, 16, and 16, for Model I, II, and II, respectively. Estimated error bounds for each parameter are as follows: *N* ±20%; *R* ±0.02 Å; $\Delta\sigma^2$ ±20%; ΔE_0 ±20%. [b] Model with lowest *Goodness of fit*, but *R* value of Ta–Si$_{\text{support}}$ Shell out of reasonable range. [c] Recommended Model. [d] Long contribution from SiO_2 support.

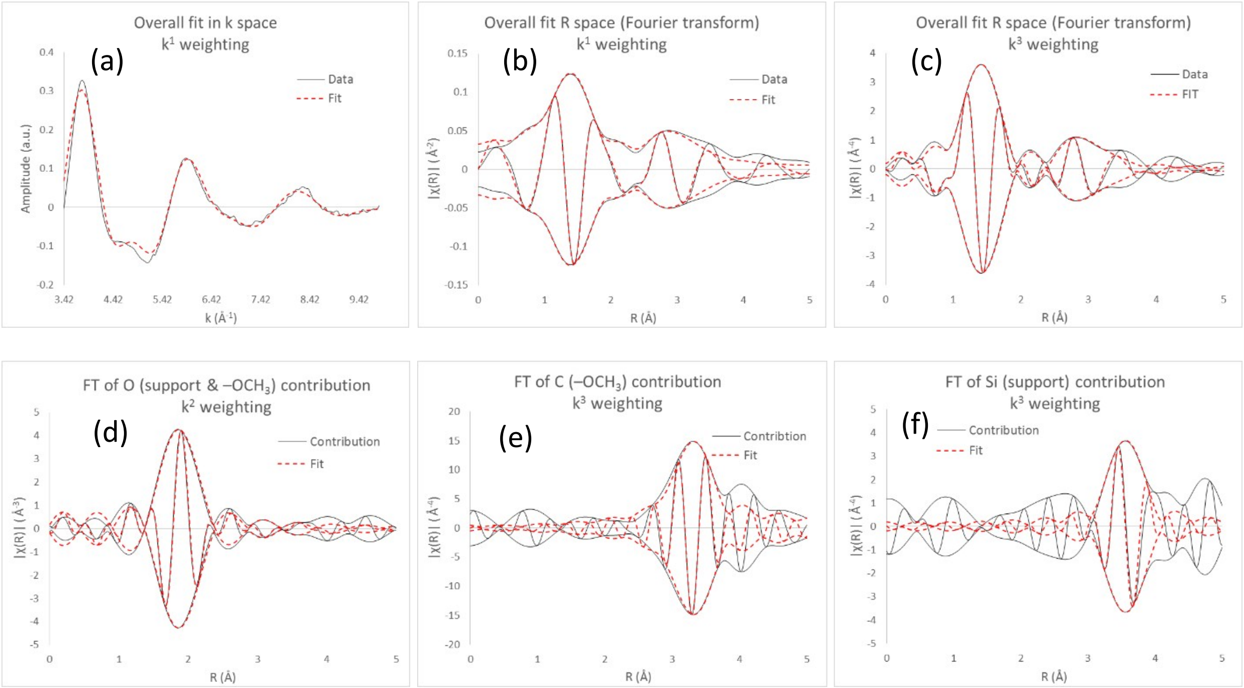

Figure S28. Fitted model I for EXAFS data characterizing Ta complex **2A** formed by supporting $Ta_2(OMe)_{10}$ on SiO_2-700. (a) k^1-weighted EXAFS function and overall fit; (b) k^1-weighted Fourier transform of the EXAFS function and overall fit; (c) k^3-weighted Fourier transform of the EXAFS function and overall fit; (d) k^2-weighted Fourier transform of residual data and modeled contribution of the Ta–$O_{methoxy/support}$ shell; (e) k^3-weighted Fourier transform of residual data and modeled contribution of the Ta–$C_{methoxy}$ shell; (f) k^3-weighted Fourier transform of residual data and modeled contribution of the Ta–$Si_{support}$ shell.

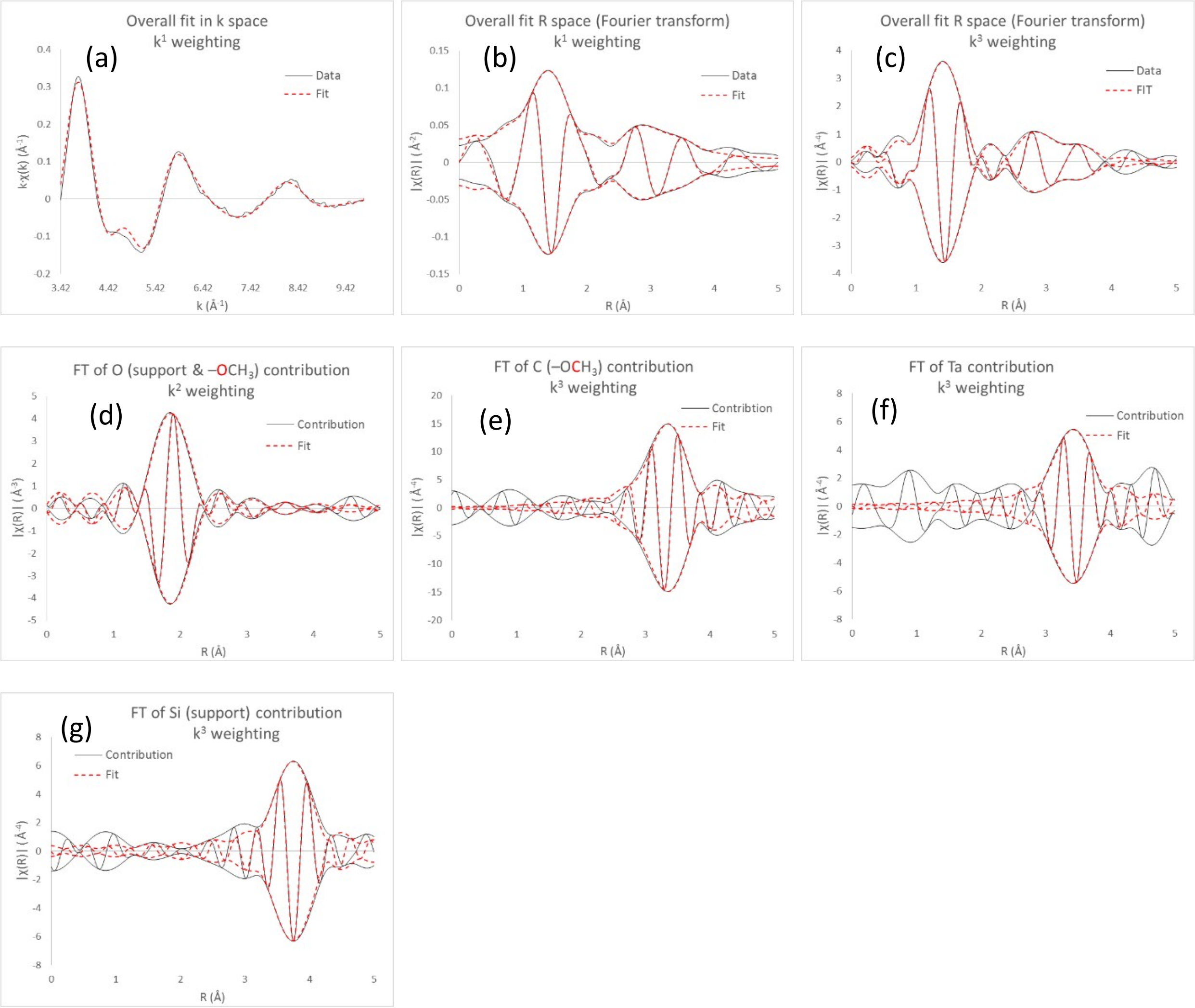

Figure S29. Fitted model II for EXAFS data characterizing Ta complex **2A** formed by supporting $Ta_2(OMe)_{10}$ on SiO_2-700. (a) k^1-weighted EXAFS function and overall fit; (b) k^1-weighted Fourier transform of the EXAFS function and overall fit; (c) k^3-weighted Fourier transform of the EXAFS function and overall fit; (d) k^2-weighted Fourier transform of residual data and modeled contribution of the Ta–$O_{methoxy/support}$ shell; (e) k^3-weighted Fourier transform of residual data and modeled contribution of the Ta–$C_{methoxy}$ shell; (f) k^3-weighted Fourier transform of residual data and modeled contribution of the Ta–Ta shell; (g) k^3-weighted Fourier transform of residual data and modeled contribution of the Ta–$Si_{support}$ shell.

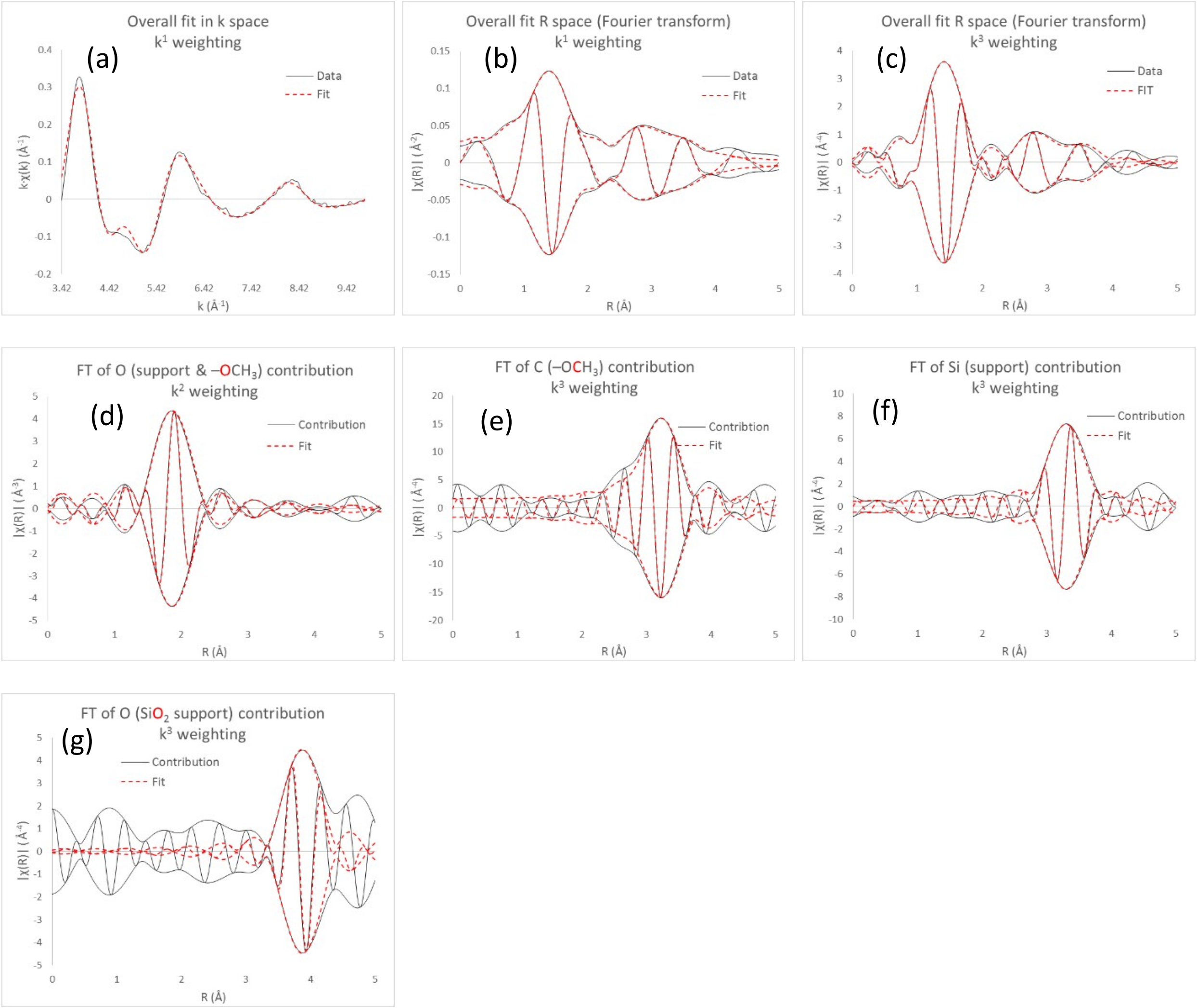

Figure S30. Fitted model III for EXAFS data characterizing Ta complex **2A** formed by supporting $Ta_2(OMe)_{10}$ on SiO_2-700. (a) k^1-weighted EXAFS function and overall fit; (b) k^1-weighted Fourier transform of the EXAFS function and overall fit; (c) k^3-weighted Fourier transform of the EXAFS function and overall fit; (d) k^2-weighted Fourier transform of residual data and modeled contribution of the Ta–$O_{methoxy/support}$ shell; (e) k^3-weighted Fourier transform of residual data and modeled contribution of the Ta–$C_{methoxy}$ shell; (f) k^3-weighted Fourier transform of residual data and modeled contribution of the Ta–$Si_{support}$ shell; (g) k^3-weighted Fourier transform of residual data and modeled contribution of the Ta–O_{long} shell.